Chapter 5: The Hydrodynamical Riemann Problem

5.1) Introduction

5.1.1) General Introduction to the Riemann Problem

We have seen in Chapter 4 that even Burgers equation, the simplest non-linear scalar conservation law, can give rise to complex flow features such as shocks and rarefactions. Linear schemes were seen to be inadequate for treating such problems. In Chapter 3 we realized that a simple non-linear hybridization introduced by TVD limiters could yield a monotonicity preserving reconstruction. In Sub-section 4.5.2 we even designed an approximate Riemann solver for evaluating consistent and properly upwinded numerical fluxes at zone boundaries based on the HLL flux for scalar conservation laws. Such a strategy for obtaining a physically sound flux can indeed be extended to systems to yield a basic second order accurate scheme. Since better fluxes translate into better schemes, in this Chapter we invest a little time to understand strategies for obtaining a good, high-quality, physically consistent flux at the zone boundaries for use in numerical schemes. In this chapter we restrict attention to the Euler equations. However, the next Chapter will show that the insights gained here are of great importance in designing good strategies for obtaining the numerical flux at zone boundaries in numerical schemes for several hyperbolic conservation laws of interest in several areas of science and engineering.

In this and the next paragraph we motivate the need for studying the hydrodynamical Riemann problem. Assume that we are solving a problem on a one-dimensional mesh with fluid variables defined at the zone centers. The best choice of fluid variables in simple Cartesian geometries consists of the density, the momentum densities in each direction and the total energy density. These variables are referred to as *conserved variables* and are an optimal choice because they enable us to enforce local mass, momentum and energy conservation. Recall the Lax-Wendroff theorem from Sub-section 4.7 which states that conservation form ensures that shocks move at the correct speed and converge to the right locations on a mesh. The choice of variables is not

constraining because we can derive equivalent *primitive variables* from these conserved variables. A good choice of such primitive variables could be the density, pressure and velocities. We can use our slope limiters to endow each flow variable in each zone with a linear profile. The limiters can be applied to the conserved variables but it is slightly more advantageous to apply them directly to the primitive variables. Limiting the primitive variables enables us to put in a small check to ensure that the density and pressure profiles are positive all over each zone of the mesh. (The positivity of the density is assured in one dimension by the TVD limiting if the initial density is positive. Because the pressure is a derived variable, its positivity is not ensured by a TVD limiting procedure that is applied to the total energy density. In Chapter 7 we will see how we can reconstruct the conserved variables while still retaining pressure positivity.) The primitive variables are also the variables of choice in which the expressions for shock and rarefaction fans are expressed. Once linear profiles have been constructed in each zone, we can use the zone-centered variables and their linear slopes to obtain the flow variables to the left and right of any given zone boundary, see eqn. (3.55). Call the variables to the left of a certain zone boundary $\left(\rho_{1L}, v_{x1L}, v_{y1L}, v_{z1L}, P_{1L} \right)$ and call the corresponding flow variables to the right of the same zone boundary $\left(\rho_{1R}, v_{x1R}, v_{y1R}, v_{z1R}, P_{1R} \right)$. We want to obtain a set of flow variables at the zone boundary from which we can evaluate the consistent and properly upwinded numerical flux.

The flow variables that enable us to calculate a physically consistent numerical flux at the zone boundary are referred to as the *resolved state*. The nomenclature is consistent with that developed in Sub-sections 3.4.3 and 4.5.1. But how should we obtain the resolved state? Instinctively, one might want to derive a resolved state by taking an arithmetic average of the left and right variables above. If the jump in flow variables is small, the use of an arithmetic average might even be adequate. For very small jumps in flow variables, one might also imagine the fluctuations in the flow variables propagating along the characteristics of the flow, as shown in Sub-section 1.5.2. Our study of rarefaction shocks in the Burgers equation in Sub-Section 4.5.1 has shown us that using an arithmetically averaged solution to compute a numerical flux can yield entropy

violating solutions when the initial conditions are discontinuous. Thus the physically consistent fluxes that we use at zone boundaries should satisfy an *entropy condition*. In general, the jump in densities $\rho_{1L} - \rho_{1R}$, velocities $v_{x1L} - v_{x1R}$ and pressures $P_{1L} - P_{1R}$ can be very large if the flow has one or more discontinuities. Early insight on this problem was obtained by Bernhardt Riemann who analyzed the problem of how flows develop when we have two adjacent slabs of fluid with a discontinuity in flow variables across them. The problem considered by Riemann (1860) is referred to as the *Riemann problem* and is a standard building block in numerical schemes for compressible flow. Sections 3.4 and 4.5 have prepared us for this study by showing us the importance of the Riemann problem for linear hyperbolic problems and scalar conservation laws. The hydrodynamical Riemann problem is the object of our study in this Chapter.

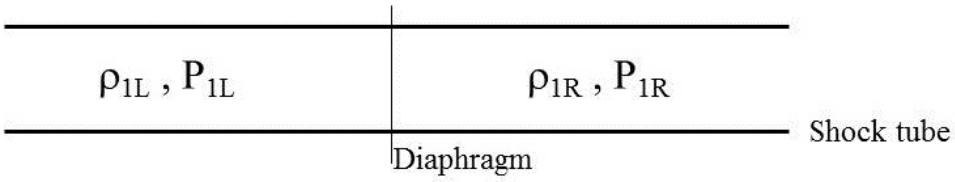

Fig. 5.1 shows the initial conditions in a shock tube before the diaphragm is removed.

A mechanical instantiation of the problem considered by Riemann consists of a *shock tube*. Such shock tubes are routinely used to study flows with shocks and the physics of shock waves. A shock tube consists of a long slender tube with a diaphragm in the middle. Initially, the volume to the left of the diaphragm is filled with gas having density and pressure ρ_{1L} and P_{1L} respectively while volume to the right of the diaphragm is filled with gas having density and pressure ρ_{1R} and P_{1R} respectively. At some point, the diaphragm is suddenly removed and we wish to know the subsequent flow features that develop. A schematic diagram of the initial conditions before the diaphragm is removed is provided in Fig. 5.1, where we only show the central portion of the shock tube. We readily see that, but for permitting arbitrary velocities v_{x1L} and v_{x1R} to the left and right, the shock tube problem is very similar to the problem that interests us in this Chapter.

Riemann's ingenious realization was that even though the problem involved strong jumps in density, pressure and possibly velocity, the resolution of the discontinuity would bear some imprint of the linearized problem with some important differences. The linearized version of the problem being discussed would only have infinitesimally small jumps in flow variables. From Sub-section 1.5.2 and Fig. 1.9 we already know that the linearized problem with very small fluctuations that are localized at a point along the x-axis would resolve itself into : **i)** *a right-going sound wave*, **ii)** *a left going sound wave* and **iii)** *an entropy wave* between them. The entropy wave may well have an additional shear in the transverse velocities across it. The shear is brought on by the fact that v_{y1L} may differ from v_{y1R} and similarly for v_{z1L} and v_{z1R}. Riemann realized that the fully non-linear problem (i.e. with arbitrary jumps in flow variables across the diaphragm) would resolve itself into: **i)** *a right-going shock wave or rarefaction fan*, **ii)** *a left-going shock wave or rarefaction fan* and **iii)** *an entropy pulse* which may well have an additional shear in the transverse velocities. When we studied compressive waves for scalar conservation laws with convex fluxes in Sections 4.2 and 4.3, we learned that they steepen into shocks. Similarly, Sections 4.2 and 4.4 showed us that situations which correspond to an initial rarefaction open up into rarefaction fans. The connection between the linearized problem and the fully non-linear problem for the Euler equations (which too have a convex flux) can be made very concrete by realizing that : **i)** A finite amplitude right-going sound wave can self-steepen into a right-going shock or open out to form a right-going rarefaction wave depending on its initial profile. **ii)** A finite amplitude left-going sound wave can self-steepen into a left-going shock or open out to form a left-going rarefaction wave depending on its initial profile. **iii)** An entropy wave, being *linearly degenerate*, can have any entropy jump across it. (Linearly degenerate waves are waves that flow with the same speed regardless of wave amplitude. I.e., unlike shocks an entropy pulse does not self-steepen.) When the entropy jump across an entropy wave becomes large, the wave becomes an entropy pulse. Let us illustrate a Riemann problem with a right-going shock, a left-going rarefaction fan and a contact discontinuity between the two. A schematic depiction of the propagation of characteristics in space and time in is shown in Fig. 5.2. We see that the solution is self-similar. In the course of this Chapter we will show that Fig. 5.2 depicts the result of removing the diaphragm in Fig.

5.1 in the situation where $P_{1L} > P_{1R}$ and $\rho_{1L} > \rho_{1R}$. An entropy pulse is also often referred to as a *contact discontinuity*.

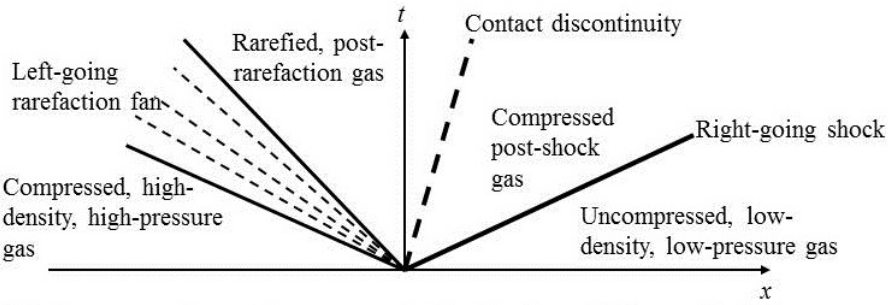

Fig. 5.2 shows a schematic representation in the x-t plane of a Riemann problem with a right-going shock, a left-going rarefaction fan and a contact discontinuity between the two. The figure depicts the result of removing the diaphragm in Fig. 5.1 in the situation where $P_{1L} > P_{1R}$ and $\rho_{1L} > \rho_{1R}$.

5.1.2) Introducing The Riemann Problem as a Building Block for Numerical Schemes

The connection between the Riemann problem and its utility in numerical methods for computing flows with potentially discontinuous solutions was made very slowly in the scientific literature. Godunov (1959) wrote a paper in which he viewed flow variables in each zone of a mesh as being slabs of fluid. The slabs would obviously have discontinuities between them at the zone boundaries. Godunov suggested that the Riemann problem should be used to obtain a resolved state at each zone boundary. His important insight was that fluid fluxes computed with the help of that resolved state would naturally be physically consistent and properly upwinded. This is because the Riemann problem represents an "in the small" evolution of the actual initial discontinuity. A one-dimensional schematic representation of Godunov's method is shown in Fig. 5.3. Zone-centered variables are indicated with an integer subscript "*i*" and variables at zone boundaries are indicated by a half-integer subscript "*i*+1/2". Time levels are indicated by a superscript "*n*" that denotes the n^{th} time step. Intermediate values of variables that are used to take a complete time step can have fractional superscripts. On either side of zone number 1 we show the solution of the Riemann problem where right- and left-going

shocks are shown as $S_{\rightarrow}$ and $S_{\leftarrow}$ respectively, right- and left-going rarefaction fans are shown as $R_{\rightarrow}$ and $R_{\leftarrow}$ respectively and the contact discontinuity is shown as C_0 . It can be broken up into the following two conceptual steps for taking a time step Δt on a one-dimensional mesh with zones of size Δx :

i) Discretize the conservation law $\partial_t U + \partial_x F(U) = 0$ as slabs of fluid that have a flat profile within each zone. Thus within each zone "*i*" at a time $t^n = n\,\Delta t$ we have a vector of conserved variables $\overline{U}_i^n$.

ii) Solve the Riemann problems at zone boundaries to get the resolved states and resolved numerical fluxes, i.e. at zone boundary "*i*+1/2" we have $F_{RP}\left(\overline{U}_i^n, \overline{U}_{i+1}^n\right)$. Use them to make the update

$$\overline{U}_i^{n+1} = \overline{U}_i^n - \frac{\Delta t}{\Delta x}\left(F_{RP}\left(\overline{U}_i^n, \overline{U}_{i+1}^n\right) - F_{RP}\left(\overline{U}_{i-1}^n, \overline{U}_i^n\right)\right) \qquad (5.1)$$

Section 5.4 will explain to us how the resolved state, i.e. the state that coincides with the boundary, can be obtained from the Riemann problem. Section 5.4 will also explain to us how the resolved fluxes are computed at each zone boundary.

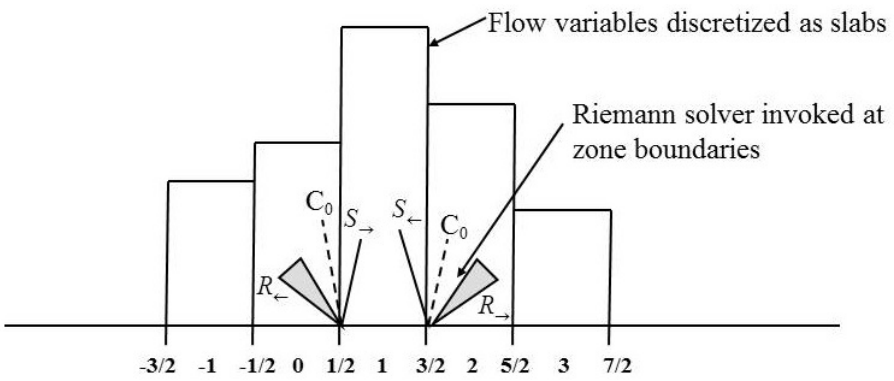

Fig. 5.3 shows a one-dimensional schematic of Godunov's method. Zone-centers are indicated by an integer and zone boundaries are indicated by a half-integer . On either side of zone number 1 we show the solution of the Riemann problem where right- and left-going shocks are shown as $S_{\rightarrow}$ *and* $S_{\leftarrow}$ *respectively, right- and left-going rarefaction fans are shown as* $R_{\rightarrow}$ *and* $R_{\leftarrow}$ *respectively and the contact discontinuity is shown as* C_0 .

Godunov's method, despite the appeal of its transparently physical interpretation, was slow in gaining wide-spread acceptance. In truth, the Riemann problem had to be solved iteratively and the iterative method proposed by Godunov was slow to converge. This made the scheme slower than other competitive schemes from that era. Furthermore, the method was only first order accurate in space and time making it very dissipative. As a result, Godunov's method languished for another two decades. In a tour de force, van Leer (1977,1979) proposed a second order extension of Godunov's scheme. van Leer's papers have been cited thousands of times and a detailed reading of those papers has continued to provide fresh insights to subsequent generations of computationalists.

It is said that the Wright brothers' invention of the aeroplane was a consequence of their making a combination of leading edge advances that meshed together harmoniously. Similarly, van Leer made the following cutting edge advances all at once:

i) A very efficient iterative solution strategy for solving the hydrodynamical Riemann problem which is still used with only small changes.

ii) A strategy for using piecewise-linear, monotonicity preserving reconstruction of the sort studied in the previous chapter. As a result each interpolated fluid variable has a linear profile within each zone. This makes the scheme spatially second order accurate

in regions of smooth flow and simultaneously enables it to capture shocks without producing spurious oscillations.

iii) A method for increasing the temporal accuracy to second order.

Later on, van Leer later realized that second order temporal accuracy could also be achieved by using the second order Runge-Kutta time-stepping strategy that was catalogued in Sub-Section 3.6.2, (van Leer 1984). van Leer's scheme is shown schematically in Fig. 5.4.

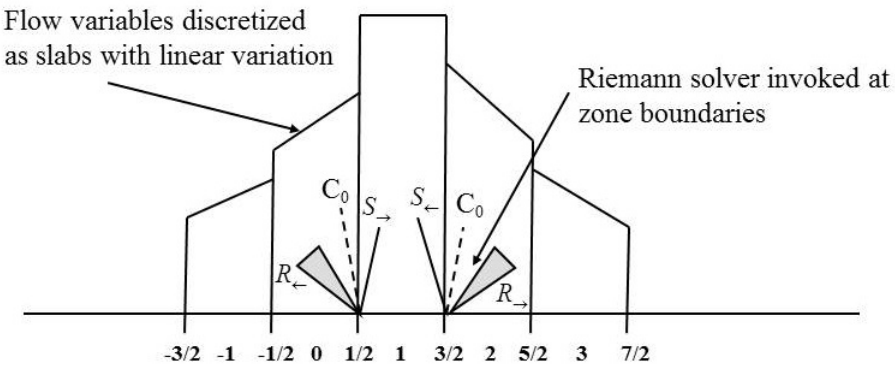

Fig. 5.4 provides a schematic representation of van Leer's scheme. Notice that the flow variables now have a linear profile within each zone, making the spatial representation of the flow variables second order accurate.

van Leer's scheme, with several modifications, is still used as a blueprint for several successful numerical codes. A possible variant of his scheme that achieves its temporal accuracy using a strategy that is simpler than the one originally presented by van Leer is described schematically below. It can be broken up into the following three conceptual steps for taking a time step Δt on a one-dimensional mesh with zones of size Δx :

i) Use a second order Runge-Kutta scheme described in eqns. (3.50) or (3.51) to achieve second order accuracy in time. The scheme has been written in a format that makes its conservative form self-evident. Each of the stages in the scheme consists of using the following two steps.

ii) Within each zone "*i*" at the start of each stage we have a vector of conserved variables $\overline{\mathrm{U}}_i$. Use this vector of conserved variables to obtain a vector of primitive

variables V_i in each zone. The vector of primitive variables consists of density, the three velocity components and the pressure. For each of the stages, make linear profiles ΔV_i within each zone for the density, velocities and pressure using the componentwise limiting applied to the vector of primitive variables, see eqn. (3.57) for an example of componentwise limiting. Do this using the limiters described in Sub-Section 3.2. Giving each slab of fluid a piecewise linear profile makes the method a spatially second order accurate shock-capturing scheme. The interpolation, which is piecewise linear within each zone, enables us to obtain $\left(\rho_{1L}, v_{x1L}, v_{y1L}, v_{z1L}, P_{1L} \right)^T \equiv V_i + \Delta V_i / 2$ and $\left(\rho_{1R}, v_{x1R}, v_{y1R}, v_{z1R}, P_{1R} \right)^T \equiv V_{i+1} - \Delta V_{i+1} / 2$ at the zone boundary "*i+1/2*", see eqn. (3.55) for an example. We calculate the left and right states at each zone boundary. Notice that the linear profiles within each zone can only be meaningfully interpreted within the zones in which they are defined. This is what produces a jump in the flow variables at the zone boundaries. The presence of the jump in fluid variables at zone boundaries enables the hydrodynamical Riemann problem to introduce the needed dissipation. Recall that in Sub-section 4.5.2 we showed that the jump in the scalar variable at the zone boundaries was essential if we wanted the approximate Riemann solver to stabilize discontinuities. The same concept carries over to systems of conservation laws.

iii) Using the left and right flow variables at each zone boundary, compute the resolved state and resolved flux at each zone boundary. The resolved flux is indeed the properly upwinded and consistent numerical flux that we wish to use in our scheme. The Riemann solver described in this chapter can be used like a machine that accepts a left and right state and produces a numerical flux. The numerical flux can then be used to obtain the time update for each of the stages shown in either eqn. (3.50) or (3.51).

By the end of this chapter the reader should be able to understand the construction of a flow solver that is similar to the one described in the previous paragraphs using the codes provided in this book. Problem 5.4 provides a step by step guide for constructing a one-dimensional flow solver that is based on the steps described above.

It is worth pointing out that the texts by Courant & Friedrichs (1948) and Landau & Lifshitz (1987) provide a very detailed study of hydrodynamical shocks and rarefactions. Texts by Ben-Artzi and Falcovitz (2003) and Toro (2009) study the hydrodynamical Riemann problem in great detail, especially as it applies to numerical schemes. Colella and Glaz (1985), Menikoff and Plohr (1989), Ben-Artzi (1989) and Ben-Artzi and Birman (1990) present ingenious solutions to the Riemann problem in the presence of real gas equations of state and reactive flow. In this chapter, we only present the essentials that are needed to study the numerical solution of the Riemann problem.

In Sec. 5.2 we study hydrodynamical shocks, in Sec. 5.3 we study hydrodynamical rarefaction fans and Sec. 5.4 we study the hydrodynamical Riemann problem including strategies for its iterative solution. The reader is also given a foretaste of the more modern Riemann solvers for the Euler and MHD systems that will be described in Chapter 6. The Riemann solver that we describe here also gives us several insights that are generally useful in designing Riemann solvers for several hyperbolic systems of interest to engineering and science.

5.2) Hydrodynamical Shock Waves

In Chapter 4 we saw that a non-linear scalar hyperbolic equation of the form $\partial_t u + \partial_x f(u) = 0$ can sustain shock waves. Say the values on either side of such a shock are u_1 and u_2. If the shock's propagation speed is "s", eqn. (4.10) and Fig. 4.8 tell us that the fluxes and conserved variables should satisfy the relation $f(u_1) - f(u_2) = s\,(u_1 - u_2)$. We saw there that the derivation of this expression was very simple and general because it only depended on a two-dimensional integration over a small rectangular domain in one spatial coordinate and time, see Fig. 4.8. If the shock travelled a distance "X" in a time "T", the domain was chosen such that it contained the discontinuity. Thus it is very easy to see that the same expression should hold component-wise for a hyperbolic system of equations in conservation form. A construction that parodies eqn. (4.9) and Fig. 4.8 for a system of conservation laws bears out our anticipation. In this section we focus

attention on the one-dimensional Euler equations that can be written in conservation form as:

$$\frac{\partial}{\partial t}\begin{pmatrix} \rho \\ \rho\, v_x \\ \rho\, v_y \\ \rho\, v_z \\ \varepsilon \end{pmatrix} + \frac{\partial}{\partial x}\begin{pmatrix} \rho\, v_x \\ \rho\, v_x^2 + P \\ \rho\, v_x\, v_y \\ \rho\, v_x\, v_z \\ (\varepsilon + P)\, v_x \end{pmatrix} = 0 \qquad (5.2)$$

Here ρ is the density; v_x , v_y and v_y are the velocities; P is the pressure; "e" is the thermal energy density and $\mathcal{E}$ is the total internal energy density. Notice that eqn. (5.2) can be written in the conservation form $\partial_t U + \partial_x F(U) = 0$. The equations can be solved along with the closure relation

$$\mathcal{E} = e + \frac{1}{2}\rho\, \mathbf{v}^2 \qquad \text{with} \qquad e \equiv \frac{P}{\Gamma - 1} \qquad (5.3)$$

which we take quite simply to pertain to a polytropic gas with polytropic index Γ . We wish to find the relations that hold for the fluid variables on either side of a hydrodynamical shock.

Notice that since each of the five components in eqn. (5.2) are required to satisfy eqn. (4.9) with the same shock speed $s = X/T$, we expect to find further relationships between the fluid variables on either side of a shock. In general, we anticipate the relationships to be rather complicated. Consequently, in Sub-section 5.2.1 we evaluate the conditions that relate the fluxes on either side of a fluid discontinuity in the rest frame of the discontinuity. In Sub-section 5.2.2 we obtain some relationships that pertain to shocks without regard to the fluid's equation of state. In Sub-section 5.2.3 we specialize to polytropic gases and obtain relationships between the flow variables on either side of a shock viewed in its own rest frame. Relying on the fact that the Euler system is Galilean

invariant, we obtain general relationships between the flow variables on either side of a moving shock in Sub-section 5.2.4. Several other interesting hyperbolic systems can be written in a conservation form that resembles eqn. (5.2). Consequently, the ensuing Sub-sections are peppered with several asides that highlight the similarities and differences between the Euler system and these other systems of interest.

5.2.1) Hydrodynamical Discontinuities and Shock Jump Conditions

As pointed out in the previous paragraphs, it is easiest to start our study of hydrodynamical discontinuities in the rest frame of the discontinuity. Notice that eqn. (4.9) should hold componentwise for all the components of the vector of conserved variables and the flux vector in eqn. (5.2). In such a rest frame, $s = X/T = 0$ in eqn. (4.9) and we obtain the particularly simple condition

$$\left[F(U_1) - F(U_2)\right] = 0 \tag{5.4}$$

which is to be applied to each of the five components of the flux in eqn. (5.2). Here U_1 and U_2 denote the five-component vectors of conserved variables from eqn. (5.2) that are specified on either side of the discontinuity. Our decision to work in the rest frame of the discontinuity can be justified by realizing that the Euler equations are Galilean invariant. In that frame we can specify the flow variables in primitive form on either side of the discontinuity by the vectors $\left(\rho_1, u_{x1}, u_{y1}, u_{z1}, P_1\right)^T$ and $\left(\rho_2, u_{x2}, u_{y2}, u_{z2}, P_2\right)^T$ respectively. In this section the velocities in the rest frame of the discontinuity are denoted by "u" instead of "v" to show clearly that they pertain to a specific choice of coordinate frame. The velocities in the two frames of reference are related by a Galilean transformation. Balancing the mass, momentum and energy fluxes from eqn. (5.4) yields:

$$\rho_1 \, u_{x1} = \rho_2 \, u_{x2} \tag{5.5}$$

$$\rho_1 \, u_{x1}^2 + P_1 = \rho_2 \, u_{x2}^2 + P_2 \tag{5.6}$$

$$\rho_1 \, u_{x1} \, u_{y1} = \rho_2 \, u_{x2} \, u_{y2} \tag{5.7}$$

$$\rho_1 \, u_{x1} \, u_{z1} = \rho_2 \, u_{x2} \, u_{z2} \tag{5.8}$$

$$\rho_1 \, u_{x1} \left(\frac{1}{2} \, \mathbf{u}_1^2 + h_1 \right) = \rho_2 \, u_{x2} \left(\frac{1}{2} \, \mathbf{u}_2^2 + h_2 \right) \tag{5.9}$$

Here "h" is the specific enthalpy, i.e. the enthalpy per unit mass. It is defined by

$$h = \frac{e + P}{\rho} \tag{5.10}$$

and for a polytropic gas it is given by

$$h = \frac{\Gamma}{\Gamma\text{-}1} \, \frac{P}{\rho} \tag{5.11}$$

The first natural solution to eqns. (5.5) to (5.9) consists of setting the mass flux across the discontinuity to zero. Thus we have $\rho_1 \, u_{x1} = \rho_2 \, u_{x2} = 0$. Since the densities are non-zero we have $u_{x1} = u_{x2} = 0$, i.e. there is no mass flowing through the discontinuity. Eqn. (5.6) gives us $P_1 = P_2$ so that the pressures are required to match up across this type of discontinuity. We further see from eqns. (5.7) and (5.8) that the differences in the transverse velocities $u_{y1} - u_{y2}$ and $u_{z1} - u_{z2}$ are unconstrained and can take on any value. Similarly, the difference in densities $\rho_1 - \rho_2$ is also unconstrained across this type of discontinuity. Since the pressures match up across this discontinuity while the density can undergo any arbitrary change we realize that we have a jump in entropy across this type of discontinuity. We, therefore, refer to this type of discontinuity as an entropy pulse or a contact discontinuity. Analogous to the simple waves discussed

in the previous chapters, the contact discontinuity is one of the simple wave solutions for the Euler equations.

Using the eigenmodal analysis of the Euler equations from Sub-section 1.5.2 gives us a further perspective on the discontinuities that we discussed in the previous paragraph. In that chapter we saw that very small amplitude fluctuations in the density and transverse velocities could propagate with the flow speed as entropy waves and shear waves respectively. We see that an entropy pulse consists of a discontinuous jump in entropy and is, therefore, a finite amplitude version of an entropy wave. When the transverse velocities are also discontinuous across the discontinuity, we realize that we have a finite amplitude shear pulse across the discontinuity. Again, our eigenmodal analysis of the Euler equations informs us that these pulses in fluid shear are finite amplitude versions of the shear waves studied in Chapter 1. Collectively, we refer to these fluctuations in density and transverse velocity as *contact discontinuities*. Recall though that the pressure and normal velocity must match up exactly on either side of a contact discontinuity, We have therefore demonstrated that fluctuations in the density and transverse velocities across a contact discontinuity do not self-steepen and any finite amplitude fluctuation in just these variables can propagate unchanged. We call such waves *linearly-degenerate waves* to distinguish them from the *genuinely non-linear waves*, like the sound waves in Euler flow, which can self-steepen to form shocks. Fig. 5.5 provides a schematic representation of a contact discontinuity viewed in the rest frame of the discontinuity.

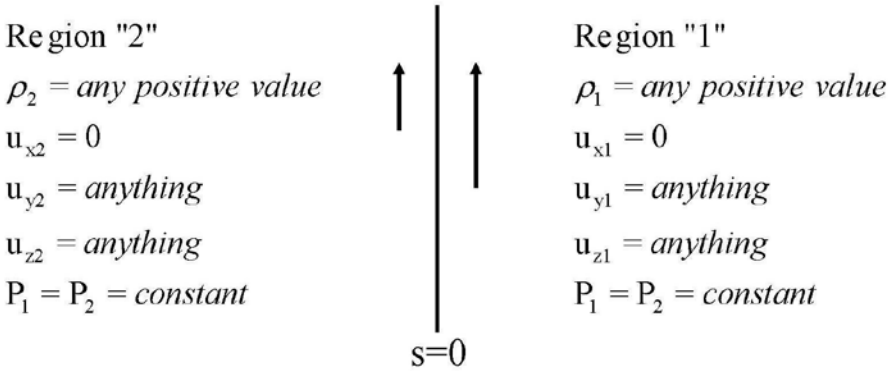

Fig. 5.5 shows the jump in fluid dynamical variables across a contact discontinuity. The variables are viewed in the rest frame of the discontinuity. The vertical arrows are meant to suggest an arbitrary jump in the transverse velocity.

Let us now consider discontinuities which have a non-zero mass flux across the discontinuity, i.e. from eqn. (5.5) we get $\rho_1 u_{x1} = \rho_2 u_{x2} \neq 0$. Eqns. (5.7) and (5.8) for the balance of the transverse momentum fluxes immediately give us $u_{y1} - u_{y2} = 0$ and $u_{z1} - u_{z2} = 0$. Because we are in the rest frame of the discontinuity, we make the further simplifying assumption that

$$u_{y1} = u_{y2} = u_{z1} = u_{z2} = 0 \tag{5.12}$$

Eqns. (5.5) and (5.6) for the conservation of mass and x-momentum remain unchanged but (5.9) for energy conservation then simplifies to give us:

$$\frac{1}{2} u_{x1}^2 + h_1 = \frac{1}{2} u_{x2}^2 + h_2 \tag{5.13}$$

Eqns. (5.5), (5.6), (5.12) and (5.13) give us the conditions that prevail in the rest frame of a normal shock. The shock is called “normal” because the transverse velocities are zero. These equations, which are essentially balance equations on the fluid fluxes, are also referred to in the literature as the *shock jump conditions* or the *Rankine-Hugoniot jump conditions* after Rankine (1870) and Hugoniot (1889) who first derived them and studied

them in detail. Since shocks emerge through self-steepening of sound waves, it is natural to think of shocks as the non-linear extension of sound waves studied in Chapter 1. In one dimension it is natural to talk about right- and left-going sound waves and consequently of right- and left-going shocks. Unshocked fluid flows into a right-going shock from the right and into a left-going shock from the left. Fig. 5.6 shows schematic diagrams for right- and left-going shocks viewed in the rest frame of the shock. For the rest of this chapter, variables that are subscripted by "1" indicate fluid that propagates into a shock or rarefaction fan while variables that are subscripted by a "2" indicate fluid that is on the other side of the shock or rarefaction fan. Analogous to the simple waves discussed in the previous chapter, shocks constitute another kind of simple wave solution for the Euler equations.

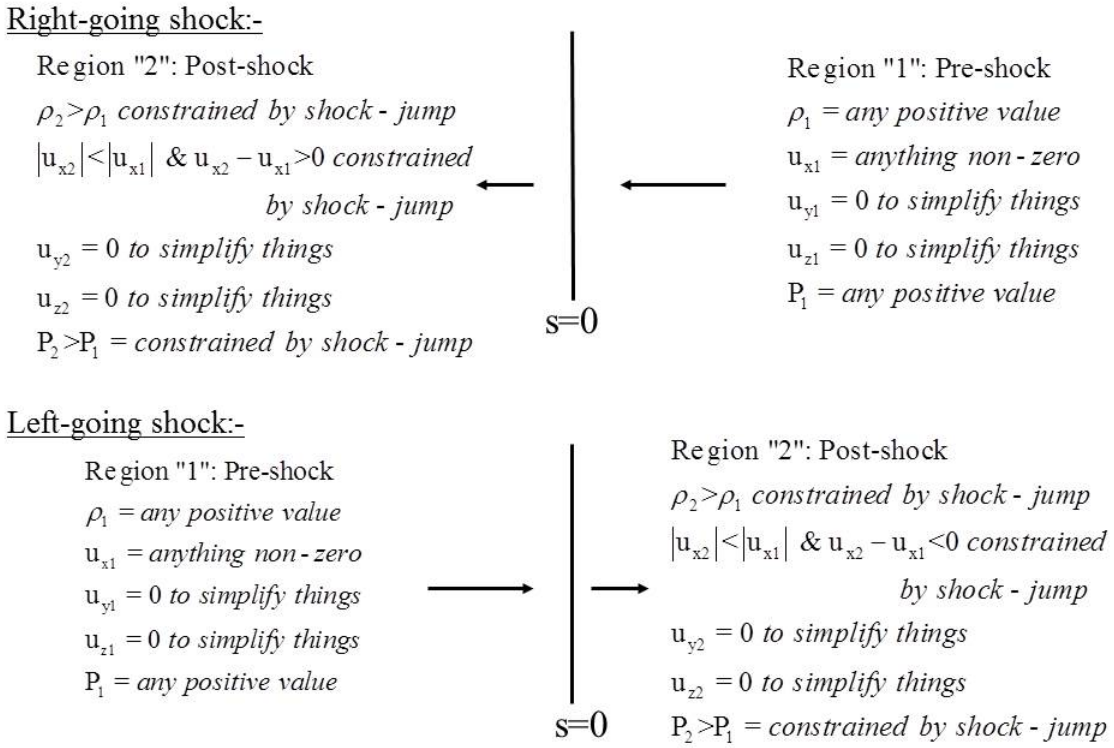

Fig. 5.6 shows the jump in fluid dynamical variables across shocks. The variables are viewed in the rest frame of the shocks. The horizontal arrows are meant to suggest normal velocity jumps.

It is very interesting to make connections between hydrodynamical shocks and the material that we have studied in the previous two chapters. We make such a connection in

this paragraph. As with our study of the Burgers equation in Chapter 4, it is possible to have discontinuities in hydrodynamical flow that will not evolve to form shocks. For the Burgers equation we saw that certain initial discontinuities actually go on to form rarefaction fans. For the Burgers equation, the entropy condition, see Section 4.4, determines whether an initial discontinuity goes on to form a shock or a rarefaction; an exactly analogous situation prevails for the Euler equations. When studying linear systems of hyperbolic equations in Chapter 3 we further learned that the variables on one side of a simple wave are related to the variables on the other side by a single parameter, see Sub-section 3.4.2. The same is true for simple waves, i.e. isolated shocks and rarefaction fans, arising from the Euler system. We will discuss hydrodynamical rarefaction fans in the next section. To be physically realizable, an isolated hydrodynamical shock should also raise the entropy of the fluid that flows through it; recall our discussion of entropy in Sub-section 4.2.2 and Section 4.3. To determine the direction of propagation of a one-dimensional shock, a simple rule of thumb is to "follow the entropy". Physically consistent hydrodynamical shock waves always raise the entropy in the post-shock region.

Because we expect a shock to represent a pile-up of material, we also expect the post-shock density ρ_2 to be greater than the density ρ_1 in the unshocked fluid; recall our mechanistic model of shock waves in Section 4.2. Since the entropy is proportional to $\log\left(\mathrm{P}/\rho^{\Gamma}\right)$ we can therefore conclude that the post-shock pressure and temperature are greater than the corresponding pressure and temperature in the unshocked fluid. Problem 5.1 at the end of this chapter makes this assertion more concrete. Using $\rho_2 > \rho_1$ we can also obtain important insights into the fluid velocities in the shock's rest-frame. Eqn. (5.5) which represents mass conservation, consequently implies that $\left|\mathrm{u}_{\mathrm{x2}}\right| < \left|\mathrm{u}_{\mathrm{x1}}\right|$ and also that u_{x1} and u_{x2} have the same sign, trends that are also displayed in Fig. 5.6. We also see from Fig. 5.6 that $\mathrm{u}_{\mathrm{x1}} < 0$ in the rest-frame of a right-going shock while $\mathrm{u}_{\mathrm{x1}} > 0$ in the rest-frame of a left-going shock.

We saw in Chapter 4 that characteristics flow into a physically realizable shock, resulting in the loss of information at a shock. Problem 5.2 at the end of this chapter shows that characteristics of a given family flow into a shock of the same family. Thus if we have a right-going shock, the characteristics $v_{xL} + c_{sL}$ from the left of the shock and $v_{xR} + c_{sR}$ from the right side of the shock flow into the shock. In other words, a right-going shock is the locus of converging C_+ characteristics formed by eigenvalues $\lambda = v_x + c_s$. Similarly, a left-going shock is the locus of converging C_- characteristics formed by the eigenvalues $\lambda = v_x - c_s$. In that sense, information is indeed lost at hydrodynamical shocks. Once a hydrodynamical shock forms in a problem, it may be impossible to uniquely retrieve the initial conditions that gave rise to it.

Shocks and Entropy Generation

We very briefly turn our attention to the physical process of entropy generation at shocks. While the Euler equations are quite often a reasonably good representation for several flow problems, it is important to realize that they basically represent the inviscid limit of the Navier-Stokes equations which indeed include the viscous terms. Within a shock, the viscous terms in the Navier-Stokes equations are very important in raising the entropy in the post-shock fluid. The text by Landau & Lifshitz (1987) shows how a viscous flow profile with a finite width reduces to a discontinuous shock jump in the limit where the viscosity tends to zero, thus making the connection between the Navier-Stokes and Euler equations very clear. The viscous terms in the momentum and energy equations are proportional to the second derivative of the velocity. Thus while the viscous terms are negligible in smooth flow, they can become rather large at a shock-front due to the rapid change in velocity across the shock front. Consequently, the viscous terms operate in a thin layer around the shock. Several numerical schemes for shock-capturing, especially those with an older vintage, try to reproduce the same physical process by including some amount of *artificial viscosity*. The artificial viscosity is then designed to stay small everywhere except at locations where shocks are detected.

The important question is: How big should this artificial viscosity be? To answer that question, consider fluid flow taking place with a typical velocity "v" in a region having a size characterized by "L". Let the mean sound speed be "c_s" and let the mean free path of the molecules be "l". The viscosity "η" will scale as, $\eta \sim c_s\, l$. The Reynolds number, Re , scales as $Re \sim (v\ L)/(c_s\ l)$. Now say that the flow is supersonic so that a shock develops in it. Far from the shock, we have $Re>>1$ so that viscosity is unimportant. When we focus on the shock though, the characteristic size over which the shock forms is given by $L \sim l$. As a result, in the vicinity of the shock, we have $Re \sim 1$. Now say that a problem is being solved on a computational mesh with zones of size Δx . If we want to capture shocks with a typical size that is a few zones wide, we will require the Reynolds number to be of order unity on length scales that are comparable to the width of the shock. As a result, the numerical viscosity will have $\eta \sim v\, \Delta x$ in the vicinity of the shock.

The current trend is to move away from such artificial viscosity-based schemes and rely on the self-adjusting properties of the Riemann solver to produce the correct amounts of entropy and dissipation at discontinuities. However, the Riemann solver that we construct later on in this chapter will itself use shocks as one of its building blocks and will thus implicitly incorporate the physical dissipation and consequent entropy generation that takes place at shocks. Furthermore, as we will see later, even such Riemann solver-based higher order Godunov schemes are best off if they are supplemented by a very small amount of artificial viscosity. The artificial viscosity is not needed for one-dimensional shock flow but it is needed to provide cross-stream coupling at multi-dimensional shocks, (Quirk 1994) .

The discussion in this sub-section has shown that strong shocks have larger jumps in their flow variables. As a result, the physical viscosity generates entropy more efficiently at stronger shocks with the result that stronger shocks have smaller viscous widths than weaker shocks, as shown by Thomas (1944). We see the same trend in numerical schemes where a very weak shock can sometimes be spread across several zones but a strong shock will steepen to have a width of one or two zones. By itself this

fact is not detrimental for modern schemes for fluid flow though it can have an adverse effect when radiative processes also cause strong changes in the post-shock temperature and pressure. In such situations it may be appropriate to take time steps that are governed both by the Courant condition as well as the time scale for radiative cooling on the computational mesh.

The discussion in this sub-section has also shown us that the strength of a shock depends on the extent to which entropy is raised at a shock. In the remaining sub-sections it will help to have a measure of the strength of a shock. Thus any tracer of this entropy increase, such as the ratio of post-shock to unshocked pressures P_2 / P_1, is a good tracer of the strength of a shock. In the next few sub-sections we will liberally use the ratio of pressures as a measure of shock strength.

Comparing Linearly Degenerate Waves for the Euler and MHD Equations

The entropy pulse that arises for the Euler equations can also have an associated shear wave. This is symptomatic of the fact that the eigenvectors with eigenvalues given by $\lambda = v_x$ in the Euler system permit an entropy wave as well as a pair of shear waves. This leads to a degeneracy in the eigenvalues. Such waves do not self-steepen as they propagate in space. They are, therefore, known as linearly degenerate waves as opposed to genuinely non-linear waves , i.e. the sound waves, which do steepen as they propagate. Consequently, one can have any amount of jump in the density or transverse velocity across a contact discontinuity without having a change in the propagation speed of the discontinuity. Compare that to a hydrodynamical shock wave, where increasing in the post-shock pressure (with the pre-shock conditions held constant) causes the shock to propagate faster into the unshocked gas.

The MHD equations also sustain an entropy wave. If the magnetic field is non-zero in the direction of wave propagation, then such an entropy wave cannot sustain a shear in the transverse velocities across it. This is because the magnetic field breaks the

degeneracy of eigenvalues noted above. For the MHD system, the torsional Alfven waves carry the shear in the flow. The MHD system then has one entropy wave and two Alfven waves as its linearly degenerate waves while the four magnetosonic waves are nonlinear. The two fast magnetosonic waves are precise analogues of hydrodynamical sound waves. As the magnetic field strength is reduced to zero, the fast magnetosonic waves will even transition in a continuous fashion to the sound waves while the Alfven waves transition continuously to the shear waves.

5.2.2) The Hugoniot Adiabat

In Sub-section 3.4.2 we saw that the values on one side of a simple wave are related to the values on the other side by a single parameter, the coefficient of the right eigenvector. In the same spirit, given a specification of the pre-shock density ρ_1 and pressure P_1 and a measure of the strength of the shock, say P_2 / P_1, we wish to predict the other thermodynamic variables in the post-shock region. We would also like to express the rest-frame velocities u_{x1} and u_{x2} as well as their difference $u_{x2} - u_{x1}$ in terms of the above-mentioned variables. In wanting to do all this we are drawing on our intuition which tells us that for a given set of unshocked thermodynamic variables and one post-shock variable, we should be able to determine all the other post-shock thermodynamical variables and the velocity differences. Our present study of the *Hugoniot adiabat* enables us to do just that. An adiabat is just a portrait in phase space showing all the possible isolated shocks (or rarefactions) of a given family that can be connected to a certain set of unshocked variables.

The equations are simplified if we define *specific volumes* as $V_1 \equiv 1/\rho_1$ and $V_2 \equiv 1/\rho_2$. To arrive at expressions for the thermodynamical variables it also helps to initially eliminate the velocities from the problem. We also identify a *mass flux variable* "j" which is defined by $j \equiv \rho_1 u_{x1} = \rho_2 u_{x2}$. We then have

$$u_{x1} = j V_1 \quad ; \quad u_{x2} = j V_2 \tag{5.14}$$

Substituting the velocities from eqn. (5.14) in eqn. (5.6) then gives an expression of the mass flux that depends purely on the thermodynamical variables as follows:

$$\mathrm{j}^2 = \frac{\mathrm{P}_2 - \mathrm{P}_1}{V_1 - V_2} \tag{5.15}$$

Because j^2 is positive we see that we can only have one of the two following possibilities. The first possibility is $\mathrm{P}_2 > \mathrm{P}_1$ and $V_1 > V_2$. The second possibility is $\mathrm{P}_2 < \mathrm{P}_1$ and $V_1 < V_2$. Since we take subscript "1" to indicate unshocked, uncompressed gas, only the first possibility is physically consistent with entropy generation at a realizable shock. We call such shocks *compressive shocks* because they result in a pressure increase in the post-shock region. It is also possible to obtain

$$\mathrm{j} = \mp \sqrt{\frac{\mathrm{P}_2 - \mathrm{P}_1}{V_1 - V_2}} \tag{5.16}$$

where the –ve sign for the mass flux "j" pertains to right-going shocks and the +ve sign pertains to left-going shocks. See the right- and left-going shocks in Fig. 5.6 to realize that they have negative and positive mass fluxes respectively. Substituting eqn. (5.15) in the energy equation, i.e. eqn. (5.13), gives one possible expression for the Hugoniot adiabat:

$$\begin{aligned} &\mathrm{h}_1 + \frac{1}{2}\,\mathrm{u}_{\mathrm{x1}}^2 = \mathrm{h}_2 + \frac{1}{2}\,\mathrm{u}_{\mathrm{x2}}^2 \;\Rightarrow\; \mathrm{h}_1 + \frac{1}{2}\,\mathrm{j}^2\,V_1^2 = \mathrm{h}_2 + \frac{1}{2}\,\mathrm{j}^2\,V_2^2 \;\Rightarrow \\ &\mathrm{h}_1 - \mathrm{h}_2 + \frac{1}{2}\left(V_1 + V_2\right)\left(\mathrm{P}_2 - \mathrm{P}_1\right) = 0 \end{aligned} \tag{5.17}$$

Since h_2 in the above equation depends on P_2 and $\rho_2 = 1/V_2$, the above equation makes it evident that a specification of the unshocked thermodynamical variables P_1 and ρ_1 and one post-shock thermodynamical variable, i.e. P_2, then permits us to obtain the other

thermodynamical variable ρ_2. For problems involving a general equation of state, it may be more valuable to obtain eqn. (5.17) in terms of the specific internal energy defined by e / ρ. We then get

$$e_1 V_1 - e_2 V_2 + \frac{1}{2}(V_1 - V_2)(P_2 + P_1) = 0 \tag{5.18}$$

For polytropic equations of state the above equations yield several further simplifications, as we will see in the next section. Even for a general equation of state we realize that the internal energy density in the above equation depends on pressure as $e = P/(\Gamma - 1)$ with the result that given P_1 and ρ_1 and P_2 we can always obtain ρ_2 iteratively using the above equation. For most real gases, the effective polytropic index Γ is a slowly varying parameter. As a result, we can freeze it around some local value as shown in the design of the Riemann problem for real gases in Colella & Glaz (1985). To solve for the shock structure Colella & Glaz showed that one can make local iterations around the shocked state to find an approximate value of Γ.

We will make a detailed study of the hydrodynamical Riemann problem over the course of this Chapter. For that study it is very useful to have a compact expression for the velocity jump across the shock, $u_{x2} - u_{x1}$. To do that, we first obtain $u_{x2} - u_{x1} = j\,(V_2 - V_1)$ and then use eqn. (5.16) to get

$$u_{x2} - u_{x1} = \pm\sqrt{(P_2 - P_1)(V_1 - V_2)} \tag{5.19}$$

The +ve and –ve signs in the above equation pertain to right- and left-going shocks respectively. It is now easy to see that $u_{x2} - u_{x1} > 0$ for right-going shocks while $u_{x2} - u_{x1} < 0$ for left-going shocks, as also catalogued in Fig. 5.6.

Notice that none of the equations derived in this sub-section depend on the form of the equation of state. In the next section we derive further relations that are specific to the assumption of a polytropic gas.

5.2.3) Normal Shocks in Polytropic Gases

Many of the requisite insights in computational astrophysics, engineering and space physics can be gained by studying normal shocks in polytropic gases. (Even when gases are not polytropic, as is the case in the interior of a pre-supernova star or in a problem with strong combustion, they seem to approximate polytropic gases in restricted density and temperature ranges. See Zwerger & Muller (1997) or Timmes & Swesty (2000) for the equation of state for nuclear matter. For combustion problems involving gases, see Colella & Glaz (1985) and for problems involving condensed phase material equations of state, see Horie (2007).) Furthermore, in several science and engineering problems the gas does indeed satisfy a polytropic equation of state to a rather good approximation. For that reason we make an in depth study of normal shocks in polytropic gases. In this sub-section, we wish to restrict study to the flow variables in the rest frame of the shock. In the next sub-section we will remove this restriction.

Using the polytropic relation, eqn. (5.11), in eqn. (5.17) for the Hugoniot adiabat we obtain

$$\frac{\rho_1}{\rho_2} = \frac{\mathrm{u}_{x2}}{\mathrm{u}_{x1}} = \frac{V_2}{V_1} = \frac{(\Gamma+1)\ \mathrm{P}_1 + (\Gamma-1)\ \mathrm{P}_2}{(\Gamma-1)\ \mathrm{P}_1 + (\Gamma+1)\ \mathrm{P}_2} \tag{5.20}$$

Notice that eqn. (5.20) gives us the post-shock density ρ_2 in terms of the unshocked density ρ_1 and the ratio of pressures $\mathrm{P}_2 / \mathrm{P}_1$. Eqn. (5.20) therefore permits us to make the Hugoniot adiabat explicit for any choice of Γ. Fig. 5.7 shows us the Hugoniot adiabat for a gas with $\Gamma = 1.4$. The solid curve in Fig. 5.7 shows us the locus of all the density ratios ρ_2 / ρ_1 that are accessible for physically acceptable choices of pressure ratio $\mathrm{P}_2 / \mathrm{P}_1$.

Since a physical shock is always a *compressive shock*, we need $P_2 / P_1 > 1$. The dashed curve in Fig. 5.7 shows us the locus of a *rarefaction shock*. In a rarefaction shock, the entropy in the shocked gas is lower than the entropy in the unshocked gas. Thus rarefaction shocks, while mathematically feasible, are physically unacceptable because they violate an *entropy condition*. The entropy condition tells us that in place of a rarefaction shock the physical flow opens out to form a rarefaction fan. Enforcement of such an entropy condition is, therefore, of paramount importance in ensuring that a numerical scheme that is based on the Riemann problem produces physically consistent shocks and rarefaction fans. Using $T_2 / T_1 = (P_2\ V_2) / (P_1\ V_1)$ and eqn. (5.20) we can also show that

$$\frac{T_2}{T_1} = \frac{P_2}{P_1} \frac{(\Gamma+1)\ P_1 + (\Gamma-1)\ P_2}{(\Gamma-1)\ P_1 + (\Gamma+1)\ P_2} \tag{5.21}$$

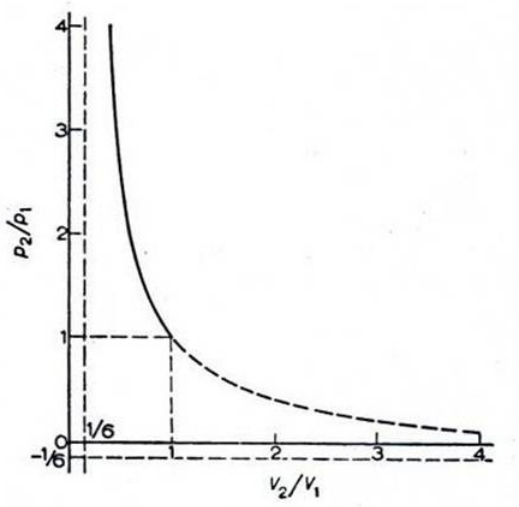

Fig. 5.7 shows us the Hugoniot adiabat for a gas with $\Gamma = 1.4$ *. The solid curve shows us the loci of all the density ratios* ρ_1 / ρ_2 *that are accessible by physically acceptable compressive shocks with* $P_2 / P_1 > 1$*. The dashed curve shows us the loci of (unphysical) rarefaction shocks. The dashed straight lines show the asymptotes of the plot. I.e., for infinitely strong shocks with* $P_2 / P_1 \rightarrow \infty$ *we have* $\rho_1 / \rho_2 \rightarrow 1/6$ *.*

We now turn to deriving relationships that pertain to the velocities in the unshocked and shocked gases as viewed in the shock's rest frame. Substituting eqn. (5.20) in (5.15) gives an expression for the mass flux in the shock's rest frame:

$$j^2 = \left[(\Gamma-1)\ P_1 + (\Gamma+1)\ P_2\right] / (2\ V_1) \tag{5.22}$$

Using $u_{x1} = j\, V_1$ and the results from eqn. (5.22) we get:

$$u_{x1}^2 = \frac{1}{2}\, V_1 \left[(\Gamma - 1)\, P_1 + (\Gamma + 1)\, P_2\right] = \frac{1}{2}\, \left(c_{s1}^2/\Gamma\right) \left[\Gamma - 1 + (\Gamma + 1)\, P_2/P_1\right] \qquad (5.23)$$

Now using $u_{x2} = V_2\, u_{x1}/V_1$ and the above equation gives:

$$\begin{aligned} u_{x2}^2 &= \frac{1}{2}\, V_1 \left[(\Gamma + 1)\, P_1 + (\Gamma - 1)\, P_2\right]^2 \Big/ \left[(\Gamma - 1)\, P_1 + (\Gamma + 1)\, P_2\right] \\ &= \frac{1}{2}\, \left(c_{s2}^2/\Gamma\right) \left[\Gamma - 1 + (\Gamma + 1)\, P_1/P_2\right] \end{aligned} \qquad (5.24)$$

In preparation for our study of the Riemann problem, it is also useful to use eqn. (5.20) in eqn. (5.19) to obtain an expression for the velocity jump $u_{x2} - u_{x1}$ as follows:

$$u_{x2} - u_{x1} = \pm\, \left(P_2 - P_1\right) \sqrt{\frac{2\, V_1}{(\Gamma - 1)\, P_1 + (\Gamma + 1)\, P_2}} \qquad (5.25)$$

The +ve and –ve signs in eqn. (5.25) pertain to right- and left-going shocks respectively.

The previous equations used the post-shock pressure as an independent variable and expressed all the other post-shock flow variables in terms of the post-shock pressure and the pre-shock flow variables. In the scientific literature, however, we often find it more convenient to use the Mach number in the unshocked gas, $M_1 = u_{x1}/c_{s1}$, as a proxy for the shock strength. We wish to derive formulae for shock relations that depend on M_1 because such formulae are often very useful in setting up isolated hydrodynamical shocks in numerical simulations. Writing eqn. (5.23) in terms of the Mach number M_1 we can then express the pressure ratio P_2 / P_1 in terms of M_1 to obtain:

$$P_2/P_1 = \left[2\,\Gamma\,M_1^2 - (\Gamma-1)\right]/(\Gamma+1) \tag{5.26}$$

Substituting eqn. (5.26) into eqns. (5.20) and (5.21) we obtain

$$\rho_2/\rho_1 = u_{x1}/u_{x2} = (\Gamma+1)\,M_1^2/\left[(\Gamma-1)\,M_1^2 + 2\right] \tag{5.27}$$

and

$$T_2/T_1 = \left[2\,\Gamma\,M_1^2 - (\Gamma-1)\right]\left[(\Gamma-1)\,M_1^2 + 2\right]/\left[(\Gamma+1)^2\,M_1^2\right] \tag{5.28}$$

Equating the pressure ratio P_2 / P_1 obtained from eqn. (5.23) and (5.24) then gives

$$M_2^2 = \left[(\Gamma-1)\,M_1^2 + 2\right]/\left[2\,\Gamma\,M_1^2 - (\Gamma-1)\right] \tag{5.29}$$

The above equations also show that in the limit where we have infinitely strong shocks, i.e. when $M_1 \to \infty$, we have the asymptotic relations

$$\frac{\rho_2}{\rho_1} = \frac{u_{x1}}{u_{x2}} \to \frac{(\Gamma+1)}{(\Gamma-1)} \;;\; \frac{P_2}{P_1} \to \infty \;;\; \frac{T_2}{T_1} \to \infty \;;\; M_2 \to \frac{(\Gamma-1)}{2\Gamma} \tag{5.30}$$

The dashed line in Fig. 5.7 shows that the ratio of densities tends to $(\Gamma+1)/(\Gamma-1)$ for extremely strong shocks. In the limit where we have strong shocks that are not necessarily of infinite strength we have the approximations

$$\frac{u_{x1}}{u_{x2}} = \frac{V_1}{V_2} = \frac{\rho_2}{\rho_1} = \frac{(\Gamma+1)}{(\Gamma-1)} \;;\; \frac{T_2}{T_1} = \frac{(\Gamma-1)}{(\Gamma+1)}\,\frac{P_2}{P_1} \;;\; u_{x1} = \sqrt{\frac{(\Gamma+1)\,P_2}{2\,\rho_1}} \;;\; u_{x2} = \sqrt{\frac{(\Gamma-1)^2\,P_2}{2\,(\Gamma+1)\,\rho_1}} \tag{5.31}$$

In Section 5.1 we saw that isolated shocks can arise in the Riemann problem. The formulae derived in this section give us a good compendium of equations pertaining to isolated shocks that we will use later in designing our Riemann solver.

Classifying discontinuities; Hydrodynamical v/s Magnetohydrodynamical Shocks

Just like the Euler equations, the one-dimensional form of the MHD equations can support shocks. In the MHD case we have four shock families; the right-going fast magnetosonic shocks, the right-going slow magnetosonic shocks, the left-going slow magnetosonic shocks and the left-going fast magnetosonic shocks. In the canonical case, these shocks follow the same foliation of waves as the linear system. The post-shock pressure is always larger than the pressure in the unshocked gas for all hydrodynamical shocks and this is also true for magnetohydrodynamical shocks. As a result, we say that all hydrodynamical shocks are compressive shocks, a property shared by MHD shocks.

In all of the formulae that we developed in this sub-section we used the ratio P_2 / P_1 as a measure of the shock strength. Similar formulae for MHD are given in the text of Jefferey & Taniuti (1964) and are adumbrated in their Appendix D, see also Bazer & Ericson (1959).

For a right-going hydrodynamical shock the C_+ characteristics formed by $\lambda = v_x + c_s$ flow into the shock from either side of the shock. Furthermore, all of the other characteristics to the right of this shock and none of the other characteristics to the left of this shock flow into the shock. Such shocks are known as *genuine* or *classical shocks*. Hydrodynamical shocks are classical because the Euler system with an ideal equation of state is convex (Lax 1972). For certain equations of state, the convexity of the Euler system cannot be guaranteed; the resulting shocks then bear further examination. A general definition of a classical shock follows: Consider an *M*-component hyperbolic conservation law with eigenvalues λ^m that are ordered from smallest to largest. Let U_L

and U_R denote the left and right states on either side of a discontinuity. The discontinuity is said to form a *classical shock of the m^{th} family* if it moves with speed "s" such that

$\lambda^{m-1}(U_L) < s < \lambda^m(U_L)$ and $\lambda^m(U_R) < s < \lambda^{m+1}(U_R)$.

I.e., notice that the characteristics of the m^{th} wave family are converging into the shock and there are only $M-1$ characteristics that are emanating from the shock. For example, see the figure below and convince yourself that the right-going shock is a classical shock. The only other discontinuities that arise for the Euler system are *linearly degenerate* contact discontinuities, also known as *exceptional discontinuities,* where characteristics of a given wave family evolve with the same speed on either side of the discontinuity. See the figure below and convince yourself that the contact discontinuity is an exceptional discontinuity. It is important to be able to classify the discontinuities that arise in a hyperbolic system of conservation laws because that information guides us in designing numerical schemes. For the Euler system with an ideal equation of state, the discontinuities are all well-behaved. Consequently, it is easy to design good numerical schemes for this system that converge to the physics of the problem.

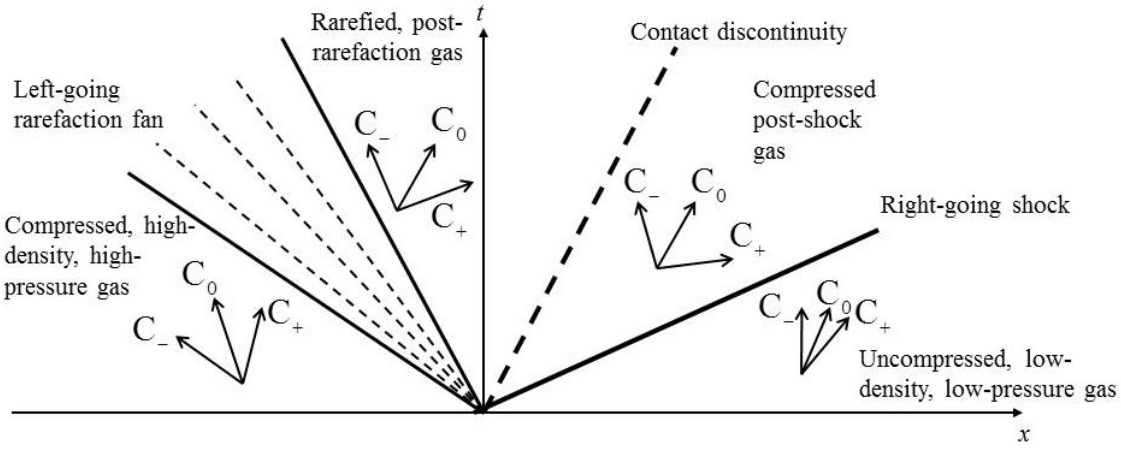

Schematic space-time diagram of a Riemann problem showing the characteristic speeds in all of the constant states. Notice that the C_+ characteristics on either side of the right-going shock propagate into the shock. The C_0 characteristics on either side of the contact discontinuity are parallel to it. The C_- characteristics on either side of the left-going rarefaction fan are parallel to the characteristics that bound the fan.

The MHD system is non-convex and can on occasion produce *compound shocks*. Recall that in the previous chapter we saw how compound shocks arise for the Buckley-Leverett equation. Consequently, degeneracies in the MHD eigenstructure can also

produce situations where characteristics from different wave families on one or the other side of a compound shock can become parallel to each other across the shock. Such compound shocks usually occur in MHD when the pressure jump is small and the transverse magnetic field on either side of a shock lies in a single plane but undergoes a change in sign across the shock. In that case it often turns out that an Alfvènic rotational discontinuity is conjoined with a magnetosonic wave, forming a compound shock.

5.2.4) Shocks in the Lab Frame

In the previous sub-section we studied normal shocks in polytropic gases. We did this in the rest frame of the shock. However, when viewed in the laboratory, the transverse velocities can have any value across a shock as long as it is left unchanged as the fluid passes through the shock. The normal velocities in the unshocked and post-shock fluids also do not need to comply with eqns. (5.23) and (5.24). In this sub-section we wish to obtain expressions for the post-shock velocity and the propagation speed of a shock in an arbitrary frame of reference. We will then demonstrate the utility of those expressions, especially as they pertain to our eventual design of a hydrodynamical Riemann solver.

Thus say that we are studying the problem of shock propagation in a frame of reference **F** where the unshocked fluid has a velocity vector given by $v_{x1}\,\hat{x} + v_{y1}\,\hat{y} + v_{z1}\,\hat{z}$ and density and pressure given by ρ_1 and P_1 respectively. The frame **F** is sometimes referred to as the lab frame. Specification of the post-shock pressure P_2 defines the strength of the shock. We can use this information in eqn. (5.23) to find the velocity u_{x1} of the unshocked fluid in the shock's rest frame. Consequently, even before we make any coordinate transformation, we know the velocity with which the unshocked fluid enters the shock in its own rest frame. We wish to transform to the shock's rest frame, denoted by $\mathbf{F}'$, because the shock jump conditions are simplest in that frame of reference. To do so, we make a Galilean transformation from the original frame of reference **F** to the frame $\mathbf{F}'$ that is moving with velocity

$\mathbf{v}_{\mathbf{F}'} = (v_{x1} - u_{x1})\hat{x} + v_{y1}\,\hat{y} + v_{z1}\,\hat{z}$ with respect to it. Since we already know u_{x1} , the velocity $\mathbf{v}_{\mathbf{F}'}$ of the frame $\mathbf{F}'$ is easy to find. See Fig. 5.8 which shows that the scalar variables remain unchanged by the transformation; however, the velocity vectors undergo transformations as shown. Fig. 5.8 also gives us the formulae for the velocity transformation as we go from one frame to the other. In the shock's rest frame, eqn. (5.24) gives us the velocity of the shocked fluid u_{x2} as a function of ρ_1, P_1 and P_2. Transforming back to the original lab frame of reference **F** (in which the shock is not a normal shock) gives us the velocity in the post-shock fluid as $(v_{x1} + u_{x2} - u_{x1})\,\hat{x} + v_{y1}\,\hat{y} + v_{z1}\,\hat{z}$. Thus if the x-component of the post-shock fluid in the lab reference frame **F** is v_{x2} we have $v_{x2} = v_{x1} + u_{x2} - u_{x1}$, with the result that $u_{x2} - u_{x1} = v_{x2} - v_{x1}$. In other words, $u_{x2} - u_{x1}$ is just the change in velocity across the shock and that change is the same regardless of the frame in which we solve the problem. We, therefore, come to the important realization that if $u_{x2} - u_{x1}$ can be specified explicitly in terms of ρ_1, P_1 and P_2 then we can specify the post-shock velocity exactly. Consequently, for a right-going shock we have:

$$v_{x2} = v_{x1} + (P_2 - P_1)\sqrt{\frac{2\,V_1}{(\Gamma - 1)\,P_1 + (\Gamma + 1)\,P_2}} \tag{5.32}$$

In the rest frame $\mathbf{F}'$, the right-going shock is at rest. It therefore propagates in the lab frame **F** with an x-velocity given by $v_{x1} - u_{x1}$. Using eqn. (5.23) for u_{x1}, we get the speed of the right-going shock as:

$$v_{shk\rightarrow} = v_{x1} + c_{s1}\sqrt{\frac{(\Gamma - 1)}{2\Gamma} + \frac{(\Gamma + 1)}{2\Gamma}\,\frac{P_2}{P_1}} \tag{5.33}$$

To see why the above two equations pertain to a right-going shock, set $v_{x1} = 0$ to realize that v_{x2} and $v_{shk\rightarrow}$ are both positive, i.e. the shock overruns the fluid to its right. Likewise, for a left-going shock we have:

$$v_{x2} = v_{x1} - (P_2 - P_1)\sqrt{\frac{2\,V_1}{(\Gamma-1)\,P_1 + (\Gamma+1)\,P_2}} \tag{5.34}$$

The left-going shock propagates in the frame F with an x-velocity given by:

$$v_{shk\leftarrow} = v_{x1} - c_{s1}\sqrt{\frac{(\Gamma-1)}{2\Gamma} + \frac{(\Gamma+1)}{2\Gamma}\,\frac{P_2}{P_1}} \tag{5.35}$$

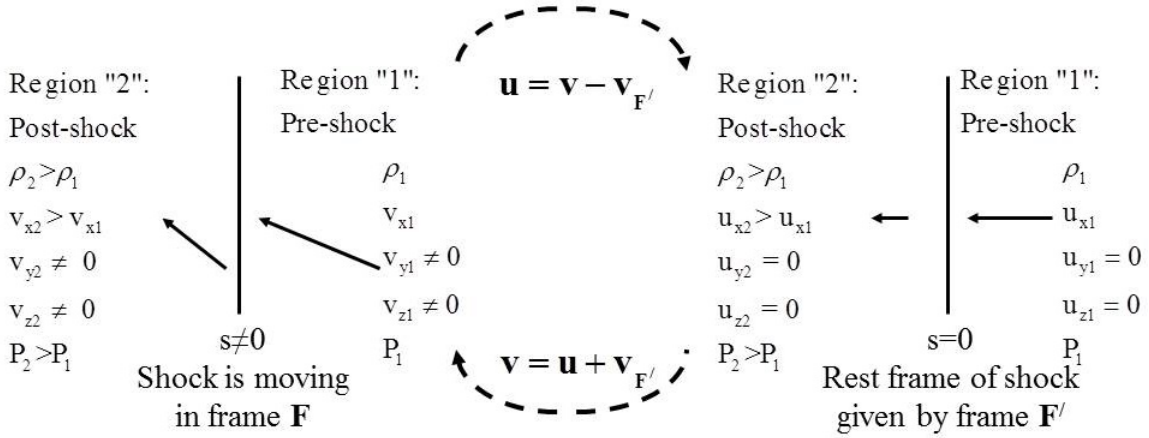

Fig. 5.8 depicts the shock in a general frame **F**. *Applying the Galilean transformation at the top takes us to the shock's rest frame* **F**′ . *The Galilean transformation shown below takes us back from frame* **F**′ *to frame* **F**. *The scalars variables remain unchanged from one frame to the other; the velocity vectors transform as shown.*

Focusing on right-going shocks, we can plot out v_{x2} using eqn. (5.32) for increasing values of pressure P_2 and any given unshocked state (ρ_1, P_1, v_{x1}). This is done in the right panel of Fig. 5.9 where the solid curve gives us the locus of all points in the (v_{x2}, P_2) plane that can be connected to the unshocked state by a right-going shock

denoted by $S_{\rightarrow}$. The analytic extension of the plot to include (unphysical) rarefaction shocks is shown via the dashed curve in Fig. 5.9. Using eqn. (5.34) we can similarly display the locus of all points in the $\left(v_{x2}, P_2 \right)$ plane that can be connected to the unshocked state by a left-going shock. The left-going shock is denoted by $S_{\leftarrow}$ and is shown in the left panel of Fig. 5.9. In that panel we again show the physical shock with a solid curve and the (unphysical) rarefaction shock as a dashed curve. We see that progressively stronger right-going shocks produce increasing (and positive) values of $v_{x2} - v_{x1}$ while progressively stronger left-going shocks produce decreasing (and negative) values of $v_{x2} - v_{x1}$.

We now make three important observations for right-going shocks:

i) $v_{x2} - v_{x1} \rightarrow \infty$ as $P_2 \rightarrow \infty$, i.e. the locus of the right-going shock is monotonically increasing in the $\left(v_{x2}, P_2 \right)$ plane.

ii) $\frac{\partial \left(v_{x2} - v_{x1} \right)}{\partial P_2} \rightarrow 0$ as $P_2 \rightarrow \infty$, i.e. the velocity increase does not keep up with the pressure increase. In fact, for $P_2 >> P_1$ we have $v_{x2} - v_{x1} \propto \sqrt{P_2}$.

iii) $P_2 = 0$ at $v_{x2} - v_{x1} = -c_{s1} \sqrt{\frac{2}{\Gamma \left(\Gamma - 1 \right)}}$, i.e there is a certain –ve velocity difference past which the pressure and density become zero in a rarefaction shock. In other words, the flow experiences a cavitation. We will see that a similar trend exists in physical rarefaction fans. The only difference is that a rarefaction fan will permit a larger range of –ve velocities before it undergoes cavitation.

Trends that are analogous to the above three points can also be specified for left-going shocks.

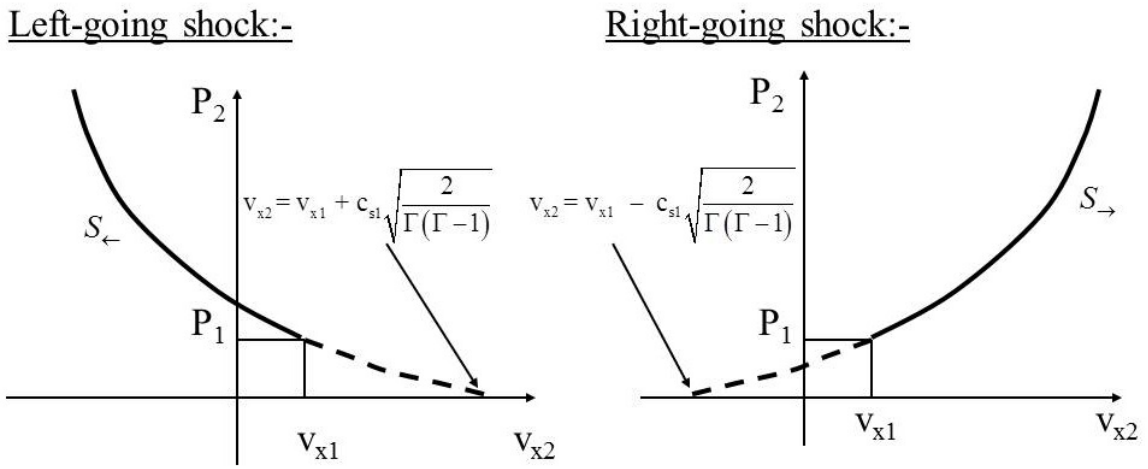

Fig. 5.9 plots out v_{x2} *for shocks with increasing values of pressure* P_2 *and any given unshocked state* (ρ_1, P_1, v_{x1}). *Left- and right-going shocks are shown with solid curves. The dashed curves show (unphysical) rarefaction shocks.*

In a numerical code, an actual rarefaction fan opens up in a self-similar fashion as we have seen before in Chapter 4. Once a rarefaction fan has opened up on a computational mesh, the jump in flow variables from one zone to the next is rather small within the rarefaction fan. Consequently, for the sake of computational simplicity, it becomes acceptable to replace actual rarefaction fans by (unphysical) rarefaction shocks. This can be done as long as an entropy fix is included in the Riemann solver to account for the fact that the rarefaction shock is actually a proxy for a rarefaction fan – a structure that spreads out in space-time. In other words, we restore physical consistency by asserting a wave model that includes an entropy fix, just as we did in Section 4.5. While unphysical, the dashed lines in the above plots nevertheless provide a reasonably good description of what happens as the flow variables evolve in a rarefaction fan. We will elaborate on this point later. Rarefaction shocks will, therefore, see use in place of rarefaction fans when constructing approximate Riemann solvers for flow codes. We will, however, not forget the central property of rarefaction fans that they preserve the entropy of the flow that passes through them, while rarefaction shocks decrease the entropy in the post-shock region. Thus while rarefaction shocks are often used in place of rarefaction fans during the iterative solution of the Riemann problem, we do need to go back post-facto and enforce an entropy fix in the approximate Riemann solver.

5.3) Rarefaction Fans

In the previous chapter we saw that self-similar solutions of a scalar conservation law can either be shocks or rarefaction fans. Inside a physical rarefaction fan, the solution was seen to be continuous. By interpreting entropy loosely in an information theoretic fashion, we realized that in a physical rarefaction fan entropy was not generated. For that reason we now focus on one dimensional continuous solutions of the Euler equations that are isentropic. While we specialize the equations in this section for ideal gases, we will also provide some general expressions for gases with real equations of state. For *isentropic flow* we have the following relations between thermodynamic variables:

$$P = P_1 \left(\frac{\rho}{\rho_1}\right)^{\Gamma} \text{ which gives : } c_s = c_{s1} \left(\frac{\rho}{\rho_1}\right)^{\frac{\Gamma-1}{2}} ; \ \rho = \rho_1 \left(\frac{c_s}{c_{s1}}\right)^{\frac{2}{\Gamma-1}} ; P = P_1 \left(\frac{c_s}{c_{s1}}\right)^{\frac{2\Gamma}{\Gamma-1}} \quad (5.36)$$

Enforcing the above relations, all of which are equivalent, enables us to pick out isentropic solutions of the Euler equations.

Using the isentropic condition allows us to drop the entropy equation $\partial_t S + \mathbf{v} \bullet \nabla S = 0$. This is equivalent to dropping the thermal energy equation, or alternatively the total energy equation, from the mix of equations we have to solve. The continuity then becomes:

$$\frac{1}{\rho}\left(\frac{\partial \rho}{\partial t} + v_x \frac{\partial \rho}{\partial x}\right) + \frac{\partial v_x}{\partial x} = 0 \quad (5.37)$$

After using $dP = c_s^2 \, d\rho$ in the momentum equation, we get

$$\left(\frac{\partial v_x}{\partial t} + v_x \frac{\partial v_x}{\partial x}\right) = - \frac{c_s^2}{\rho} \frac{\partial \rho}{\partial x} \quad (5.38)$$

Eqns. (5.36) then give us an isentropic relation $\frac{d\rho}{\rho} = \frac{2}{\Gamma - 1}\frac{dc_s}{c_s}$. Incorporating it in the above two equations gives us:

$$\frac{\partial}{\partial t}\left(\frac{2}{\Gamma - 1}c_s\right) + v_x \frac{\partial}{\partial x}\left(\frac{2}{\Gamma - 1}c_s\right) + c_s \frac{\partial v_x}{\partial x} = 0 \tag{5.39}$$

and

$$\frac{\partial v_x}{\partial t} + v_x \frac{\partial v_x}{\partial x} + c_s \frac{\partial}{\partial x}\left(\frac{2}{\Gamma - 1}c_s\right) = 0 \tag{5.40}$$

By adding and subtracting the above two equations in a suitable way, we get:

$$\left[\frac{\partial}{\partial t} + \left(v_x + c_s\right)\frac{\partial}{\partial x}\right]\left(v_x + \frac{2}{\Gamma - 1}c_s\right) = 0 \tag{5.41}$$

and

$$\left[\frac{\partial}{\partial t} + \left(v_x - c_s\right)\frac{\partial}{\partial x}\right]\left(v_x - \frac{2}{\Gamma - 1}c_s\right) = 0 \tag{5.42}$$

The self-similarity in the above two equations is worth noting. We also see that the isentropic assumption has reduced the number of variables that we need to consider in one dimension from three to two (i.e. v_x and c_s), which is a considerable simplification.

Eqn. (5.41) and (5.42) are the *characteristic equations* derived by Riemann. They tell us that the *Riemann invariant* "R" defined by

$$R \equiv v_x + \frac{2}{\Gamma - 1} c_s \tag{5.43}$$

remains constant along the C_+ characteristic curve in space-time whose trajectory is given by $\frac{dx}{dt} = v_x + c_s$. Likewise, the Riemann invariant "S" defined by

$$S \equiv v_x - \frac{2}{\Gamma - 1} c_s \tag{5.44}$$

remains constant along the C_- characteristic curve in space time with a trajectory given by $\frac{dx}{dt} = v_x - c_s$.

For a general equation of state we have

$$R \equiv v_x + l(\rho) \tag{5.45}$$

and

$$S \equiv v_x - l(\rho) \tag{5.46}$$

where

$$l(\rho) = \int_{\rho_1}^{\rho} \frac{c_s \, d\rho}{\rho} = \int_{P_1}^{P} \frac{dP}{\rho \, c_s} \tag{5.47}$$

The Riemann invariants "R" and "S" are the images of the characteristics C_+ and C_- in the two dimensional solution space (v_x, c_s).

For small fluctuations, it is easy to see that the equations derived in the previous paragraph tell us how the fluctuations move. The eigenvectors give us similar information in the limit of small fluctuations, i.e. look at eqn. (1.74) where we use the left eigenvectors defined in eqn. (1.61). We see that the fluctuations move along the characteristic curves C_+ and C_- . But the above equations also go further. They tell us that the propagation of finite amplitude isentropic fluctuations can also be tracked as long as we track them along characteristics. This process can be continued as long as the characteristics of a given wave family do not intersect, i.e. as long as shocks don't form. Fig. 5.10 shows a schematic representation of isentropic flow. The left panel shows the space-time diagram of the characteristics. The right panel shows their image in the solution space formed by the $\left(v_x, c_s \right)$ plane. From the left panel in Fig. 5.10, we see that the C_+ and C_- characteristics form an intersecting truss work and we can use it to define a coordinate system. Even if it is initially non-intuitive, let us define characteristic coordinates α and β in that coordinate system. Consider the characteristic coordinates α and β which increase in the time-like directions along the C_+ and C_- characteristics respectively as shown in the left panel of Fig. 5.10. As long as characteristics of a given family do not intersect with themselves, the two dimensional coordinate system formed by (α, β) provides an unusually easy coordinate system in which to read off the solution. In practice, the problem is implicit but say for simplicity that someone constructed a characteristic coordinate system and, furthermore, gave us $v_x(x)$ and $c_s(x)$ at time $t = 0$. Then we can find the solution at any space time point (x,t) by reading off the corresponding (α, β) from the left panel in Fig. 5.10. Then read off the Riemann invariants $R(\beta)$ and $S(\alpha)$ from the right panel of Fig. 5.10. Using $R(\beta)$ and $S(\alpha)$ and the definition of the Riemann invariants from eqns. (5.43) and (5.44), we can find $v_x(x,t)$ and $c_s(x,t)$ at any general point in space and time. In practice, constructing a characteristic coordinate system like the one shown in Fig. 5.10 is never that simple. To map the characteristics in space and time, as was done in the left panel of Fig. 5.10, we have to know the solution at all points in space and time. Thus the theoretical "solution

methodology" outlined in this paragraph assumes that the solution is already known, greatly diminishing its practical utility.

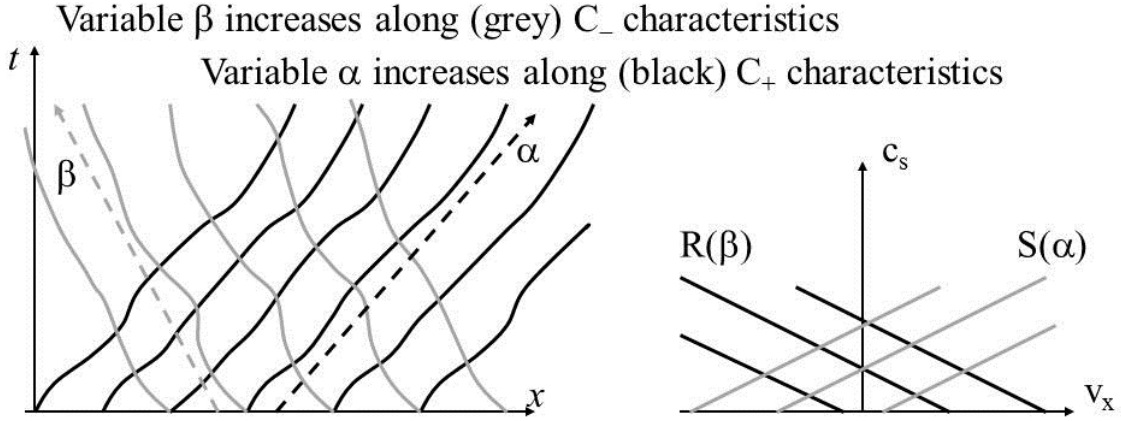

Fig. 5.10 shows a schematic representation of isentropic flow. The left panel shows the space-time diagram of the characteristics. The right panel shows their image in the solution space formed by the (v_x, c_s) *plane.*

There are, however, simple flows for which an explicit solution can be given. These simple flows take the form of compression waves and *rarefaction fans*. Out of these, we are only interested in the latter but some of the development in this section is general enough to include the former. These are *simple waves* for which either the Riemann invariant "R" or the Riemann invariant "S" is held constant all over space and time. This is tantamount to saying that the entire solution lies on only one of the straight lines in the (v_x, c_s) plane in the right panel of Fig. 5.10. As a result, v_x is always specified in terms of c_s or vice versa. In practice, this is achieved by having a constant state on one or the other side of a simple wave. A rarefaction fan usually forms next to a constant state of the flow. As a result, one of the families of characteristics has footpoints starting from the constant state of the flow. Consequently, that entire family corresponds to one and only one single value of the corresponding Riemann invariant.

The discussion in the previous two paragraphs might have been too abstract for some readers' taste; so we simplify it here. A practical, mechanical example of a rarefaction fan occurs when a piston that is initially at rest in a tube of stationary gas is

suddenly pulled out of the tube at a constant velocity. Fig. 5.11 shows a schematic diagram as well as a space-time diagram of the characteristics for the case where the piston is pulled to the left. The piston is initially located at the origin. Notice that *all* the left-going characteristics C_ must originate from the constant initial state in the gas and, therefore, must have the *same* Riemann invariant $S_1 = -2c_{s1}/(\Gamma - 1)$. Here c_{s1} is the sound speed in the initially static gas. The fluid immediately abutting the piston must move with the piston's speed. Because we know rarefaction fans to be *self-similar* solutions, they can only depend on the ratio (x/t). Since S_1 is a constant along *all* C_ characteristics, the only (isentropic) variation can be along the C_+ characteristics. The C+ characteristics are the only characteristics in this problem that can have non-trivial information propagating along them. Consequently, in order to form a self-similar solution, the C_+ characteristics must be straight lines in space-time. Note though that the density and velocity across a rarefaction fan do not have linear variation along the *x*-axis. Notice too from Fig. 5.11 that at $t = 0$ the solution has a discontinuity at $x = 0$. Over time, a wave with locus $x = c_{s1}\, t$ moves into the gas to the right. I.e. over time, more and more parcels of gas flow into the rarefaction fan from its right. We, therefore, call it a *right-going rarefaction fan.*

The right boundary of the right-going rarefaction fan shown in Fig. 5.11 is coincident with the first C_+ characteristic that varies with (x/t). In other words, the characteristic, C_+^r in Fig. 5.11, is the right-most characteristic of the right-going rarefaction fan. The left boundary of the same rarefaction fan consists of a fluid state with a velocity that matches that of the piston. That is how the right-going rarefaction fan produces a transition in x-velocities from a value of zero to its right to a value that matches the piston's velocity to its left. The space-time diagram in Fig. 5.11 shows us that the C_ characteristic are straight lines except when they pass through the rarefaction fan. Inside the rarefaction fan, the C_ characteristics can be curved. This is because they intersect different C_+ characteristics each of which carries a different value of the Riemann invariant "R".

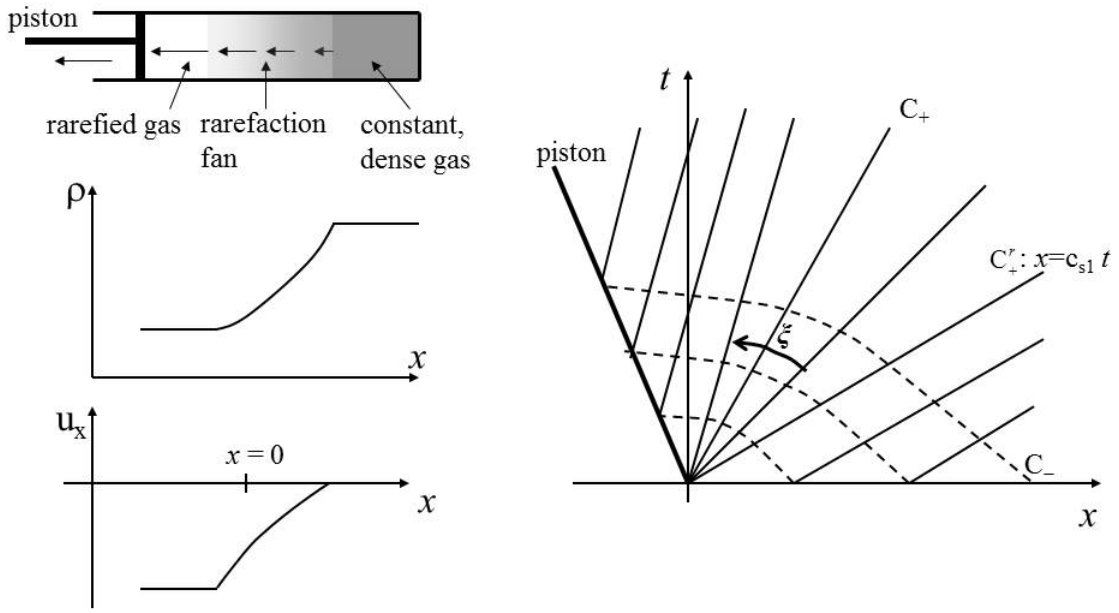

Fig. 5.11 shows how a right-going rarefaction fan develops when a piston that is initially at rest in a tube of stationary gas is suddenly pulled out of the tube at a constant velocity. The left panel shows a schematic along with plots of density and x-velocity and the right panel shows a space-time diagram of the characteristics. The piston is initially located at the origin. The thick line in the right panel shows the piston's location. The solid lines show the C_+ characteristics; the dashed lines show the C_- characteristics. The self-similarity variable ξ tags the C_+ characteristics in the right-going rarefaction fan.

In the next two sub-sections we will study right- and left-going rarefaction fans, deriving expressions that are of general computational use. The derivation of the expressions for right-going fans will be given in full while the results for the left-going rarefaction fans will be stated without further detail since they very closely parallel the previous results.

5.3.1) Right-going Rarefaction Fans

By construction, a right-going simple wave has a constant state to its right. We have seen that for right-going simple waves, the Riemann invariant $S \equiv v_x - 2\,c_s/(\Gamma - 1)$ remains constant. This holds true whether they are compression or rarefaction waves. Let us, therefore, denote the constant state to the right of this wave by a subscript "1". The flow variables in that constant state are given by

$(\rho_1, v_{x1}, v_{y1}, v_{z1}, P_1)$ with $c_{s1}=\sqrt{\Gamma P_1/\rho_1}$. Across the right-going simple wave we can then assert the constancy of the Riemann invariant "S" to get:

$$v_x - \frac{2}{\Gamma-1}c_s = v_{x1} - \frac{2}{\Gamma-1}c_{s1} \tag{5.48}$$

Eqn. (5.48) then gives us the sound speed at any point in the right-going simple wave as a function of the velocity difference $(v_x - v_{x1})$ as:

$$c_s = c_{s1} + \frac{(\Gamma-1)}{2}(v_x - v_{x1}) \tag{5.49}$$

Incorporating eqn. (5.49) into eqn. (5.36) then enables us to obtain the pressure and density in the right-going simple wave as a function of $(v_x - v_{x1})$ as:

$$P = P_1\left(\frac{c_s}{c_{s1}}\right)^{\frac{2\Gamma}{(\Gamma-1)}} = P_1\left[1 + \frac{(\Gamma-1)}{2}\frac{(v_x - v_{x1})}{c_{s1}}\right]^{\frac{2\Gamma}{(\Gamma-1)}} \tag{5.50}$$

and

$$\rho = \rho_1\left(\frac{c_s}{c_{s1}}\right)^{\frac{2}{(\Gamma-1)}} = \rho_1\left[1 + \frac{(\Gamma-1)}{2}\frac{(v_x - v_{x1})}{c_{s1}}\right]^{\frac{2}{(\Gamma-1)}} \tag{5.51}$$

Eqns. (5.49), (5.50) and (5.51) express the sound speed, pressure and density in the rarefaction or compression wave in terms of the variables in the constant state that abuts the wave and one parameter that pertains to the interior of the rarefaction fan. In eqns. (5.49) to (5.51), that controlling parameter is the velocity v_x , or alternatively, $(v_x - v_{x1})/c_{s1}$. Reasoning by analogy, recall that the post-shock pressure was the one controlling parameter that determined the structure of a shock in eqns. (5.20) to (5.25).

The above three expressions are generally true for any right-going rarefaction or compression wave in a polytropic gas. We now specialize them for a self-similar right-going rarefaction fan that emanates from $x = 0$ at $t = 0$. Since we are studying a right-going rarefaction fan, we focus on the C_+ family of characteristics. Such waves have the further special property that they obey a similarity solution that depends only on the self-similarity variable $\xi \equiv (x/t)$. Furthermore, the C_+ characteristics carry that similarity information. Setting $(x/t) = v_x + c_s$ for the right-going characteristics and using eqn. (5.49) gives us:

$$\frac{x}{t} = v_x + c_s = v_{x1} + c_{s1} + \frac{(\Gamma+1)}{2}\,(v_x - v_{x1}) \tag{5.52}$$

which can be written in an alternative form as

$$v_x - v_{x1} = -\,\frac{2}{(\Gamma+1)}\left[(v_{x1} + c_{s1}) - \left(\frac{x}{t}\right)\right] \tag{5.53}$$

Using eqn. (5.53) in (5.50) and (5.51) then gives us

$$P = P_1\left\{1 - \frac{(\Gamma-1)}{(\Gamma+1)}\,\frac{1}{c_{s1}}\left[(v_{x1} + c_{s1}) - \left(\frac{x}{t}\right)\right]\right\}^{\frac{2\Gamma}{(\Gamma-1)}} \tag{5.54}$$

and

$$\rho = \rho_1\left\{1 - \frac{(\Gamma-1)}{(\Gamma+1)}\,\frac{1}{c_{s1}}\left[(v_{x1} + c_{s1}) - \left(\frac{x}{t}\right)\right]\right\}^{\frac{2}{(\Gamma-1)}} \tag{5.55}$$

Eqns. (5.53) to (5.55) give us the internal structure of a right-going rarefaction fan that emanates from the origin at time $t = 0$. For a given right state, the flow variables in the rarefaction fan that abuts that state are entirely specified by the ratio (x/t). Notice that for a centered, right-going rarefaction fan the right-most C_+ characteristic that belongs to the fan is given by $x = (v_{x1} + c_{s1})\, t$. As one traverses the fan from right to left, $\left[(v_{x1} + c_{s1}) - \left(\frac{x}{t}\right)\right]$ increases from an initial value of zero, see the C_+ characteristic curves in Fig. 5.11. Consequently, from eqns. (5.53) to (5.55) we see that v_x , P and ρ decrease monotonically from v_{x1}, P_1 and ρ_1 as the fan is traversed from right to left. If we denote the variables to the left of a right-going rarefaction fan by $(\rho_2 , v_{x2} , v_{y1} , v_{z1} , P_2)$ we see that $v_{x2} - v_{x1} < 0$, $P_2 < P_1$ and $\rho_2 < \rho_1$. These trends run exactly opposite to the trends that we catalogued in the previous section for a right-going shock. Notice too that the transverse velocities v_{y1} and v_{z1} do not change across rarefaction fans, a trend that is shared with shocks.

Rarefaction fans are often a part of the solution to the Riemann problem at a zone boundary. We say that a C_+ rarefaction fan is open and straddles a zone boundary if $v_{x2} + c_{s2} < (dx/dt)_{boundary} < v_{x1} + c_{s1}$ where $(dx/dt)_{boundary}$ is the velocity of the boundary . When solving the Riemann problem, special attention will have to be paid to those situations where an open rarefaction fan straddles a zone boundary. Eqns. (5.53) to (5.55) are very useful when obtaining the resolved state at a moving (or stationary) zone boundary when a C_+ rarefaction fan straddles that boundary. In other words, eqns. (5.53) to (5.55) give us the interior structure of a rarefaction fan in terms of the self-similarity variable (x/t) and are, therefore, very useful for enforcing the entropy fix at a subsonic, right-going rarefaction fan.

When obtaining a numerical solution of the Riemann problem, it helps to iterate the problem towards a converged solution using one judiciously chosen iteration variable.

For shocks we see that the post-shock pressure P_2 is such a good variable. The previous paragraph has shown that the pressure P_2 behind a rarefaction fan is a similarly good variable. We, therefore, obtain expressions for $v_{x2} - v_{x1}$ and ρ_2 in terms of the variables to the right of the right-going rarefaction fan and the ratio P_2/P_1. Using eqn. (5.50) gives us

$$v_{x2} - v_{x1} = - \frac{2\, c_{s1}}{(\Gamma - 1)} \left[1 - \left(\frac{P_2}{P_1} \right)^{\frac{(\Gamma-1)}{2\,\Gamma}} \right] \tag{5.56}$$

and the isentropic condition gives us

$$\rho_2 = \rho_1 \left(\frac{P_2}{P_1} \right)^{\frac{1}{\Gamma}} \tag{5.57}$$

We can now plot out v_{x2} using eqn. (5.56) for decreasing values of pressure P_2 and any given state (ρ_1, P_1, v_{x1}) that is to the right of the right-going rarefaction. This is done in Fig. 5.12 where the solid black curve with $P_2 < P_1$ gives us the locus of all points in the (v_{x2}, P_2) plane that can be connected to the right state by a right-going rarefaction denoted by $R_{\rightarrow}$. The dashed black curve extends the same plot to the compressive side, i.e. eqn. (5.56) is plotted out even when $P_2 > P_1$. The grey curve shows us the locus of a right-going shock $S_{\rightarrow}$ that also connects to the unshocked state given by (ρ_1, P_1, v_{x1}). The solid part of the grey curve with $P_2 > P_1$ indicates a physical, compressive shock and the dashed grey curve shows the corresponding rarefaction shock. We see that for $P_2 \sim P_1$ both the black and the grey curves in Fig. 5.12 have the same slope. This is as expected. It means that for weak shocks or weak rarefaction fans it does not matter whether we use either curve. We also notice that for $v_{x2} - v_{x1} < 0$, the rarefaction fan permits a larger

velocity difference before developing a cavitation than a rarefaction shock. A flow is said to undergo *cavitation* when its pressure becomes zero. As a result, an exact Riemann solver which uses rarefaction fans and compressive shocks will fare slightly better than an approximate Riemann solver that uses compressive shocks but replaces rarefaction fans by rarefaction shocks. Such an exact Riemann solver would use the solid grey curve in Fig. 5.12 to represent right-going shocks and the solid black curve to represent right-going rarefaction fans. In practice, this represents only a small advantage because the solid black curve and the dashed grey curve in Fig. 5.12 don't differ by much. Besides, for most problems, the rarefactions in the flow are not too strong. For this reason, several approximate Riemann solvers use the shock adiabat (solid grey curve in Fig. 5.12) for compressive shocks but resort to rarefaction shocks (dashed grey curve in Fig. 5.12) to represent rarefactions. We will see in the next chapter that there are yet other Riemann solvers that resist the formation of cavitations even better than the exact Riemann solver. We also see that for $P_2 >> P_1$, i.e. for strong shocks, the rarefaction adiabat and the shock adiabat have very different asymptotic behaviors. It is for this reason that efforts to replace compressive shocks by rarefaction fans in the regime where $P_2 > P_1$ have not met with much success. For an example of such a Riemann solver which was based entirely on rarefaction fans, see Osher and Solomon (1982) and an easily implementable version of the same by Dumbser and Toro (2011).

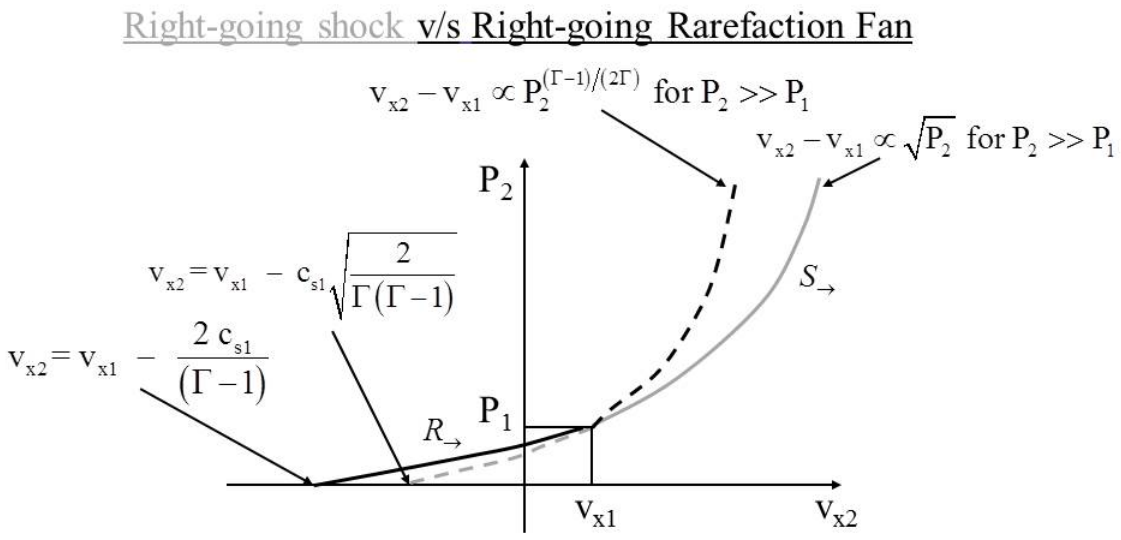

Fig. 5.12 The solid black curve shows the locus of all points that can be connected to (ρ_1, P_1, v_{x1}) *by a right-going rarefaction fan* $R_{\rightarrow}$. *The dashed black curve extends the rarefaction fan's adiabat to the compressive side. The solid grey curve shows us the locus of all right-going shocks* $S_{\rightarrow}$ *that connect to the unshocked state given by* (ρ_1, P_1, v_{x1}). *The dashed grey curve extends the shock adiabat to the rarefaction side. Only the solid grey curve and solid black curve are physically realizable. While the extended parts of the adiabats, shown with dashed curves, are not physically realizable, the text shows that they are computationally useful.*

5.3.2) Left-going Rarefaction Fans

By construction, a left-going compression or rarefaction wave has a constant state to its left. We see that for left-going compression or rarefaction waves the Riemann invariant $R \equiv v_x + 2\,c_s/(\Gamma-1)$ remains constant. As before, denote the constant state to the left of this wave by a subscript "1" and denote the flow variables in that constant state by $(\rho_1, v_{x1}, v_{y1}, v_{z1}, P_1)$. Asserting the constancy of the Riemann invariant "R" we obtain the sound speed at any point in the left-going simple wave as a function of the velocity difference $(v_x - v_{x1})$ as:

$$c_s = c_{s1} - \frac{(\Gamma-1)}{2}\,(v_x - v_{x1}) \tag{5.58}$$

We further obtain the pressure and density in the left-going simple wave as a function of $\left(v_x - v_{x1}\right)$ as:

$$P = P_1 \left(\frac{c_s}{c_{s1}}\right)^{\frac{2\Gamma}{(\Gamma-1)}} = P_1 \left[1 - \frac{(\Gamma-1)}{2} \frac{\left(v_x - v_{x1}\right)}{c_{s1}}\right]^{\frac{2\Gamma}{(\Gamma-1)}} \tag{5.59}$$

and

$$\rho = \rho_1 \left(\frac{c_s}{c_{s1}}\right)^{\frac{2}{(\Gamma-1)}} = \rho_1 \left[1 - \frac{(\Gamma-1)}{2} \frac{\left(v_x - v_{x1}\right)}{c_{s1}}\right]^{\frac{2}{(\Gamma-1)}} \tag{5.60}$$

Notice that eqns. (5.58) to (5.60) for a left-going compression or rarefaction wave are analogous to eqns. (5.49) to (5.51) for a right-going compression or rarefaction wave.

The above expressions are generally true for any left-going compression or rarefaction wave in a polytropic gas. We now specialize them for self-similar left-going rarefaction fans that are initially centered at $x = 0$. As before, we set $\left(x/t\right) = v_x - c_s$ for the right-going characteristics and using eqn. (5.58) to get

$$v_x - v_{x1} = \frac{2}{(\Gamma+1)}\left[\left(\frac{x}{t}\right) - \left(v_{x1} - c_{s1}\right)\right] \tag{5.61}$$

$$P = P_1 \left\{1 - \frac{(\Gamma-1)}{(\Gamma+1)} \frac{1}{c_{s1}} \left[\left(\frac{x}{t}\right) - \left(v_{x1} - c_{s1}\right)\right]\right\}^{\frac{2\Gamma}{(\Gamma-1)}} \tag{5.62}$$

and

$$\rho = \rho_1 \left\{ 1 - \frac{(\Gamma - 1)}{(\Gamma + 1)} \frac{1}{c_{s1}} \left[\left(\frac{x}{t} \right) - (v_{x1} - c_{s1}) \right] \right\}^{\frac{2}{(\Gamma - 1)}} \tag{5.63}$$

Eqns. (5.61) to (5.63) give us the internal structure of a left-going rarefaction fan that emanates from the origin at time $t = 0$. For a given left state, the flow variables in the rarefaction fan that abuts that state are entirely specified by the ratio (x/t). Notice that $\left[\left(\frac{x}{t} \right) - (v_{x1} - c_{s1}) \right]$ is positive and monotonically increases from zero as one traverses a left-going rarefaction fan from left to right. If we denote the variables to the right of a left-going rarefaction fan by $(\rho_2, v_{x2}, v_{y1}, v_{z1}, P_2)$ we see that $v_{x2} - v_{x1} > 0$, $P_2 < P_1$ and $\rho_2 < \rho_1$. These trends run exactly opposite to the trends that we catalogued in the previous section for a left-going shock.

We, now obtain expressions for $v_{x2} - v_{x1}$ and ρ_2 in terms of the variables to the left of the left-going rarefaction fan and the ratio P_2/P_1. Using eqn. (5.59) gives us

$$v_{x2} - v_{x1} = \frac{2\, c_{s1}}{(\Gamma - 1)} \left[1 - \left(\frac{P_2}{P_1} \right)^{\frac{(\Gamma - 1)}{2\Gamma}} \right] \tag{5.64}$$

and the isentropic condition gives us

$$\rho_2 = \rho_1 \left(\frac{P_2}{P_1} \right)^{\frac{1}{\Gamma}} \tag{5.65}$$

Eqns. (5.64) and (5.65) for a left-going rarefaction fan are analogous to eqns. (5.56) and (5.57) for a right-going rarefaction fan. Fig. 5.13 is analogous to Fig. 5.12 and compares left-going rarefaction fans, shown as $R_{\leftarrow}$, with left-going shocks. In Section 5.1 we saw that isolated rarefaction fans can arise in the Riemann problem. The formulae derived in

this section give us a good compendium of equations pertaining to isolated rarefaction fans that we will use later in designing our Riemann solver.

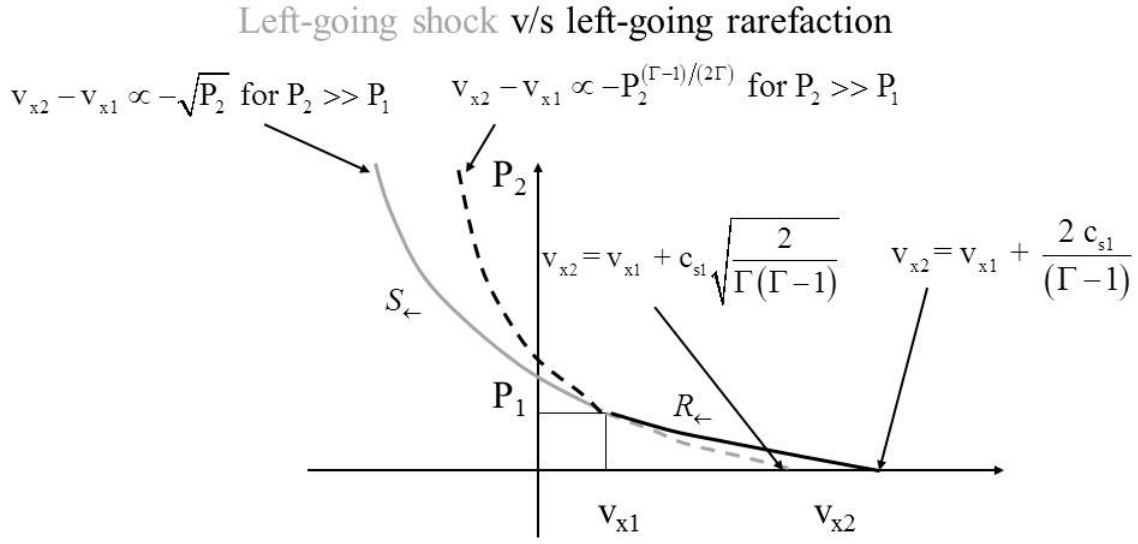

Fig. 5.13 The solid black curve shows the locus of all points that can be connected to (ρ_1, P_1, v_{x1}) *by a left-going rarefaction fan* $R_{\leftarrow}$ *. The dashed black curve extends the rarefaction fan's adiabat to the compressive side. The solid grey curve shows us the locus of all left-going shocks* $S_{\leftarrow}$ *that connect to the unshocked state given by* (ρ_1, P_1, v_{x1}). *The dashed grey curve extends the shock adiabat to the rarefaction side. Only the solid grey curve and solid black curve are physically realizable. While the extended parts of the adiabats, shown with dashed curves, are not physically realizable, the text shows that they are computationally useful.*

5.4) The Riemann Problem

In the next two sub-sections we introduce the Riemann problem in two easy stages. In Sub-Section 5.4.1 we introduce it with diagrams in the (v_x, P) plane. In Sub-Section 5.4.2 we show how the problem can be solved numerically using an iterative Newton-Raphson root solver. Sub-Section 5.4.3 describes the entropy fix in the iterative Riemann solver.

5.4.1) Intuitive Introduction to the Riemann Problem

Riemann envisioned a situation where two initially uniform slabs of gas are brought into contact at the plane $x = 0$ and then allowed to evolve self-consistently in one dimension along the x-axis. Call the initial variables to the left $\left(\rho_{1L}, v_{x1L}, v_{y1L}, v_{z1L}, P_{1L} \right)$ and call the corresponding initial flow variables to the right $\left(\rho_{1R}, v_{x1R}, v_{y1R}, v_{z1R}, P_{1R} \right)$. The Riemann problem describes the subsequent evolution of that flow. Riemann's important realization consisted of realizing that the problem can only evolve as a similarity solution in space-time. The only self-similar fluid dynamical structures that we know of are shock waves, centered rarefaction fans and contact discontinuities. In rarefaction fans the Riemann invariants are constant along certain characteristic families. Assuming that the problem is well-defined and doesn't form cavitations, Riemann asserted that there are only four possible outcomes of such a problem:

i) right-going shock and left-going rarefaction fan,

ii) left-going shock and right-going rarefaction fan,

iii) right- and left-going shocks,

iv) right- and left-going rarefaction fans.

In all of the above four cases, a contact discontinuity between the two elementary flow structures, i.e. simple waves, preserves the original sanctity of the two original slabs of fluid. Across the contact discontinuity the pressure and normal velocity remain continuous, while the density and the transverse velocities may undergo a jump. The transverse velocity remains v_{y1L} and v_{z1L} in all of the left fluid and v_{y1R} and v_{z1R} in all of the right fluid. If the two fluids in the two initial slabs have different properties, such as different polytropic indices or different composition, then that that difference is also preserved across the contact discontinuity. The previous statement would, however, have to be modified if the fluids had a complicated equation of state.

The case where $P_{1L} > P_{1R}$, $\rho_{1L} > \rho_{1R}$ with all the initial velocities zeroed is particularly interesting because of its relevance to shock tubes. The problem corresponds to Fig. 5.2 which was presented schematically in the Introduction. It is also rather simple to analyze intuitively and we do that first. Since the pressure to the left is higher, it sends

a right-going shock into the fluid to the right with a pressure P^* that is intermediate between P_{1L} and P_{1R}. All the C_+ characteristics in the left fluid will have their footpoints in the constant flow to the left of $x = 0$. Since $P^* < P_{1L}$ the only self-similar flow that can establish itself in the left fluid is a left-going rarefaction fan. The density in the post-shock gas that lies to the left of the right-going shock and the density in the gas that lies to the right of the left-going rarefaction fan will not match in general. As a result, a contact discontinuity develops in Fig. 5.2 with the same pressure P^* and x-velocity v_x^* in the two fluids on either side of it.

Fig. 5.14 is a visual representation of the solution to the Riemann problem. It shows us the four possible outcomes of the Riemann problem. Each of the four panels in the figure shows the left and right states, (v_{x1L}, P_{1L}) and (v_{x1R}, P_{1R}), along with the intermediate state (v_x^*, P^*) that connects to them. Focus on Fig. 5.14a which shows a situation that is slightly more general than the one presented in the previous paragraph. Here the left and right velocities of the initial states do not have to be zero, but their difference has to be suitably small. The right state is shown by the point (v_{x1R}, P_{1R}) and has substantially lower pressure than the left state (v_{x1L}, P_{1L}). The right state (v_{x1R}, P_{1R}) can only connect to right-going wave families. We can now identify all the right-going shocks $S_{\rightarrow}$ in the (v_x^*, P^*) plane that propagate into the unshocked gas given by (v_{x1R}, P_{1R}). This is shown by the part of the solid curve that has $P^* > P_{1R}$ in Fig. 5.14a. We also identify all the right-going rarefaction fans $R_{\rightarrow}$ in the (v_x^*, P^*) plane that propagate into the constant state given by (v_{x1R}, P_{1R}). This is shown by the part of the solid curve that has $P^* < P_{1R}$ in Fig. 5.14a. The solid curve in Fig. 5.14a is, therefore, the locus of all right-going simple waves, whether they are shocks or rarefactions, that can connect to the initial right state (v_{x1R}, P_{1R}). As a result it increases to the right, similar to the situation depicted in the Fig. 5.12 for right-going waves. If the intermediate state is

found to be $\left(v_x^*, P^*\right)$ then the right-going wave will be a shock if $P^*>P_{1R}$ and a rarefaction fan if $P^*<P_{1R}$. The left state $\left(v_{x1L}, P_{1L}\right)$ can only connect to left-going wave families. The dashed curve in Fig. 5.14a is the locus of all left-going shocks $S_{\leftarrow}$ and rarefactions $R_{\leftarrow}$ that can connect to the initial left state $\left(v_{x1L}, P_{1L}\right)$. Notice that since the dashed curve represents a left-going simple wave, it decreases to the right, similar to the situation depicted in the Fig. 5.13 for left-going waves. As before, the left-going wave will be a shock if $P^*>P_{1L}$ and a rarefaction fan if $P^*<P_{1L}$. Because the solid and dashed curves have increasing and decreasing trends respectively, the two curves are sure to intersect for any physical Riemann problem that does not produce a cavitation. The point of their intersection gives us the *intermediate state* $\left(v_x^*, P^*\right)$. Fig. 5.14a shows that the fully evolved Riemann problem has a right-going shock and a left-going rarefaction fan with a contact discontinuity between them. The density jump in the contact discontinuity has a constant pressure P^* on either side of it and moves with an x-velocity given by v_x^*. Fig. 5.15a shows the density, pressure and the x-velocity as a function of position along the x-axis of a numerically computed Riemann problem. The values of the density, pressure and velocity on the extreme left and extreme right of the plots shown in Fig. 5.15a, therefore, give us the initial left and right states of the Riemann problem. Notice from Fig. 5.15a that the left state was initialized with higher density and pressure than the right state and that the two states were stationary at the initial time. Fig. 5.2 shows the self-similar wave propagation in space and time for such a situation. Fig. 5.15a shows us that the solution indeed consists of a right-going shock and a left-going rarefaction fan along with a contact discontinuity between the two. All shocks are compressive for the Euler equations, so that the jump in the pressure shows the location of the right-going shock. The jump in the density, with a constant pressure and a constant velocity across it, shows the location of the contact discontinuity. The left-going rarefaction is identified by the continuously varying profile in the density, pressure and velocity variables. All rarefaction fans correspond to a reduction in the pressure, which enables us to figure out the direction in which the rarefaction fan propagates. We therefore see that Fig. 5.15a shows all the flow structures that we anticipate from Fig. 5.14a. This problem is known in

the literature as the Sod problem and is commonly used to verify that Euler flow codes are operating correctly.

Fig. 5.14b shows the situation where the pressure of the left state is much lower than the pressure in the right state with only a suitably small x-velocity difference between the states. We clearly see that the Riemann problem shown in Fig. 5.14b represents a right-going rarefaction fan and a left-going shock. Fig. 5.15b shows the density, pressure and the x-velocity as a function of position along the x-axis of a numerically computed Riemann problem that has a right-going rarefaction fan and a left-going shock. As before, we see that Fig. 5.15b shows all the flow structures that we anticipate from Fig. 5.14b.

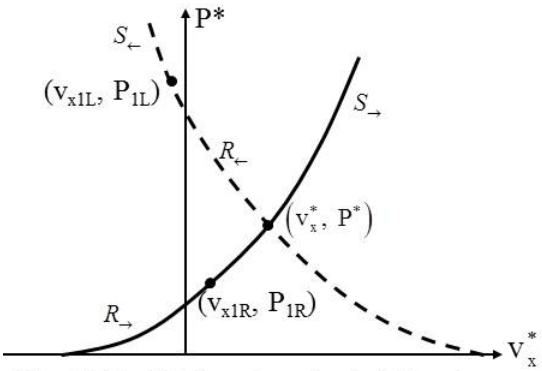

Fig. 5.14a: Right-going shock, left-going rarefaction

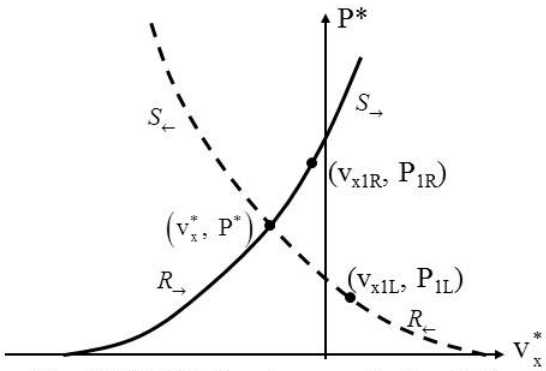

Fig. 5.14b: Right-going rarefaction, left-going shock

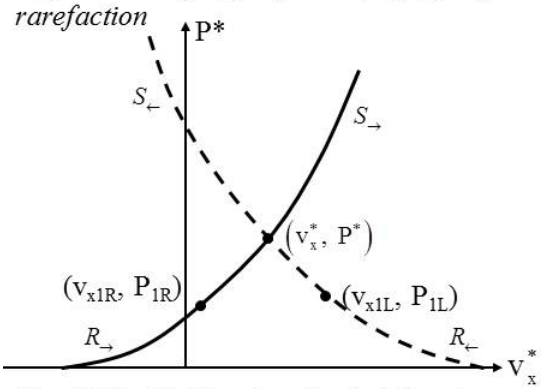

Fig. 5.14c: Right-going shock, left-going shock

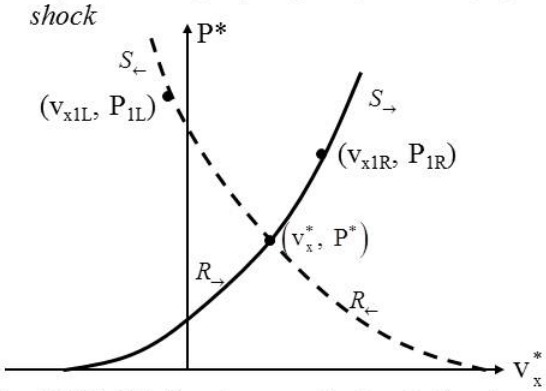

Fig. 5.14d: Right-going rarefaction, left-going rarefaction

Fig. 5.14c shows us a situation where the initial left and right states are propagating towards each other with a rather large velocity, i.e. $v_{x1L} > v_{x1R}$ so that the

fluid to the left runs into the fluid to the right. However, the difference in initial pressures between them is suitably small. In that case, the intermediate state, which is given by the point of intersection between the solid and dashed curves in Fig. 5.14c, has a pressure P^* that is greater than either P_{1L} or P_{1R}. In physical terms, the kinetic energy of the two colliding streams is turned into thermal energy. As a result, this Riemann problem resolves itself into right- and left-going shocks with a contact discontinuity between them. Fig. 5.16a shows the density, pressure and the x-velocity as a function of position along the x-axis of a numerically computed Riemann problem that has right- and left-going shocks, analogous to Fig. 5.14c. Notice that the central densities and pressures in Fig. 5.16a are much larger than the densities and pressures in the initial left or right states, thereby showing the compression that has resulted from the two colliding streams. However, the velocities of the initial left and right streams are much larger than the velocity in the central compressed region.

Fig. 5.14d shows a situation where the initial left and right states are moving apart with a rather large velocity, i.e. $v_{x1L} < v_{x1R}$ so that the fluid to the left is initially flowing away from the fluid to the right. As in Fig. 5.14c, the difference in initial pressures between the initial left and right states is suitably small. In this case the intermediate state has a pressure P^* that is less than either P_{1L} or P_{1R}. As a result, this Riemann problem resolves itself into right- and left-going rarefaction fans with a contact discontinuity between them. Fig. 5.16b shows the density, pressure and the x-velocity as a function of position along the *x*-axis of a numerically computed Riemann problem that has right- and left-going rarefaction fans, analogous to Fig. 5.14d.

A couple of computational exercises are provided at the end of this chapter. They invite the reader to build a one-dimensional flow solver for the Euler equations and use it to solve the problems shown in Figs. 5.15 and 5.16. As seen from Figs. 5.15 and 5.16, the numerical solutions are not entirely perfect and the computational exercises explain why.

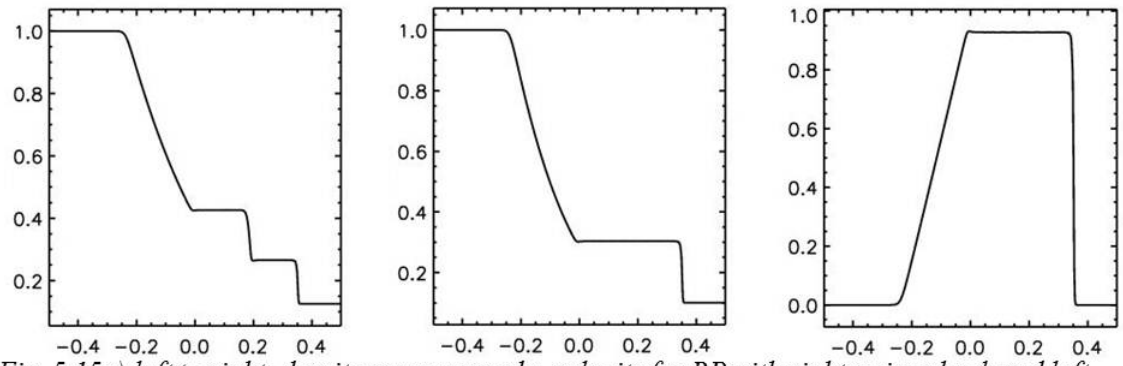

Fig. 5.15a) left to right: density, pressure and x-velocity for RP with right-going shock and left-going rarefaction

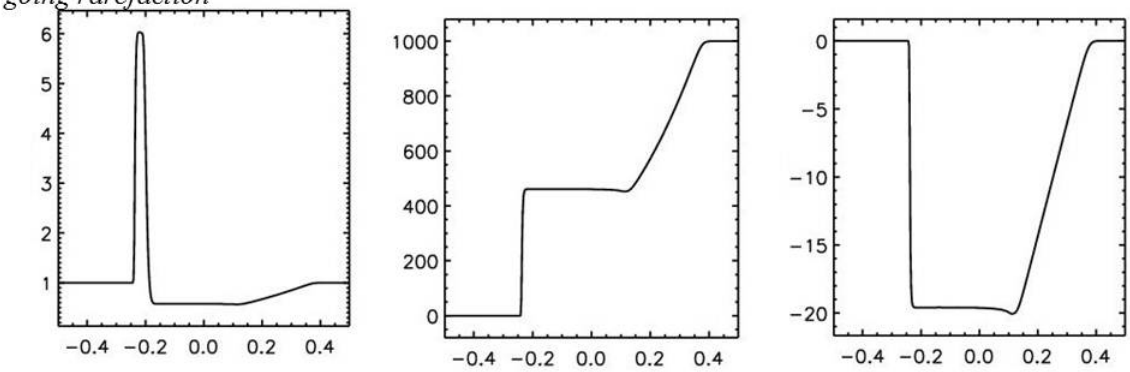

Fig. 5.15b) left to right: density, pressure and x-velocity for RP with left-going shock and right-going rarefaction

We observe from the discussion in the previous two paragraphs that in all cases, the contact discontinuity has a pressure P^* on either side of it and moves with a velocity v_x^* along the x-axis. Recall our convention that subscripts "2" are used to denote post-shock or post-rarefaction fan quantities. The solid curves in Fig. 5.14 give us the loci of all states $\left(v_{x2R}^*,\ P_{2R}^*\right)$ that connect to the initial right state $\left(\ v_{x1R}, P_{1R}\right)$ of the Riemann problem via either a right-going shock or rarefaction. The dashed curves in Fig. 5.14 give us the loci of states $\left(v_{x2L}^*,\ P_{2L}^*\right)$ that connect to the initial left state $\left(\ v_{x1L}, P_{1L}\right)$ of the Riemann problem via either a right-going shock or rarefaction. A solution strategy for resolving the Riemann problem should, therefore, consist of finding the pressure P^* for which $v_{x2L}^* = v_{x2R}^* = v_x^*$. The curves for $\left(v_{x2R}^*,\ P_{2R}^*\right)$ and $\left(v_{x2L}^*,\ P_{2L}^*\right)$, are strongly non-linear and so we realize that a solution strategy will necessarily consist of iterating on the pressure $P^* = P_{2L}^* = P_{2R}^*$ till the condition $v_{x2L}^* = v_{x2R}^*$ is satisfied. We also observe that the

solid and dashed curves in Fig. 5.14 change character as they transition from shocks to rarefaction fans. Expressing that change of character in a numerical code entails additional programming, inefficient cache usage and a possible loss of vectorization. For that reason, it has come to be standard practice in this field to replace rarefaction fans by rarefaction shocks in production codes. As seen in Section 4.5, it is very important to have an entropy fix in one's code when rarefaction shocks are used as a proxy for rarefaction fans.

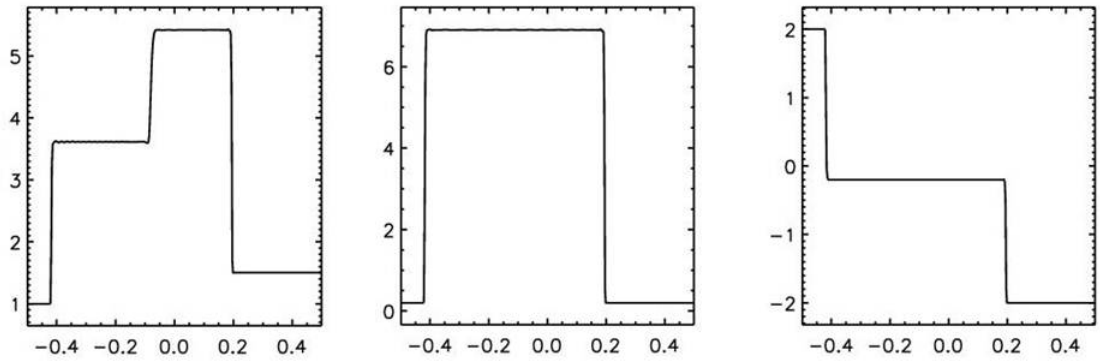

Fig. 5.16a) left to right: density, pressure and x-velocity for RP with right- and left-going shocks

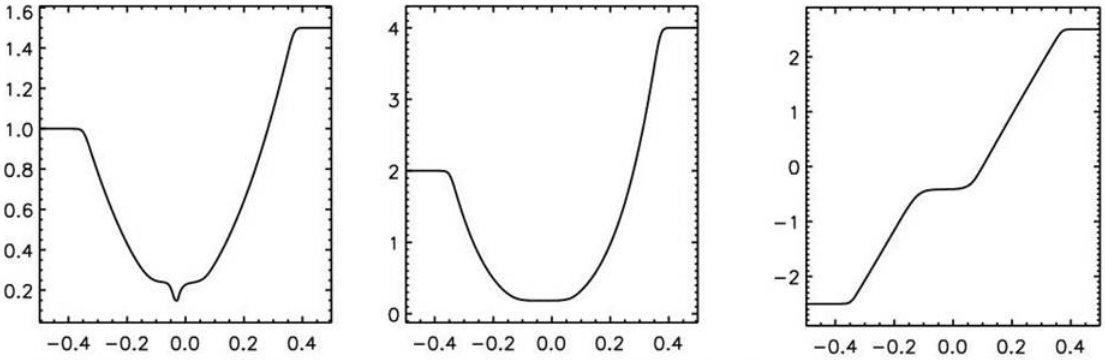

Fig. 5.16b) left to right: density, pressure and x-velocity for RP with right- and left-going rarefaction fans

5.4.2) Iterative Solution of the Riemann Problem

The previous sub-section has shown that a numerical solution of the Riemann problem consists of finding the intermediate state $\left(v_x^*,\ P^*\right)$. Once the intermediate state is found, the resolved state can also be found. Recall that the resolved state, which is the state that overlies the zone boundary in space and time in Figs. 5.3 and 5.4, yields the

consistent and upwinded numerical flux. This is the flux that we use in our numerical schemes. In this sub-section we, therefore, describe the procedure for iteratively obtaining the intermediate state.

Notice from Fig. 5.14 that for any physical left and right state, there is always a single intermediate state, thus ensuring it can always be found. Notice too that the right- and left-going adiabats shown in that figure are always continuous and differentiable, thus ensuring that efficient root finding methods for finding the intermediate state can be used. Because the curves depicted in Fig. 5.14 are not straight lines, the solution has to be obtained iteratively. In this section we explain the Newton-Raphson iterative procedure developed by van Leer (1979). As explained previously, it is often advantageous to replace rarefaction fans by rarefaction shocks as long as the wave model includes an entropy fix. As noted by Colella & Woodward (1984) and Colella (1985) such an approximate Riemann solver that is based on a *two-shock approximation* is perfectly adequate for practically all situations. For that reason, we specify "S" in equation numbers to denote that the equation can be used all by itself in an approximate Riemann solver that is based exclusively on shocks and a contact discontinuity. We will also specify "R" in equation numbers to denote that the equation pertains to rarefaction fans and can be used along with the equations for shocks to design an exact Riemann solver for hydrodynamics. Riemann solvers that are based exclusively on rarefaction fans (Osher and Solomon 1982) have not been very successful because they cannot handle very strong shocks properly.

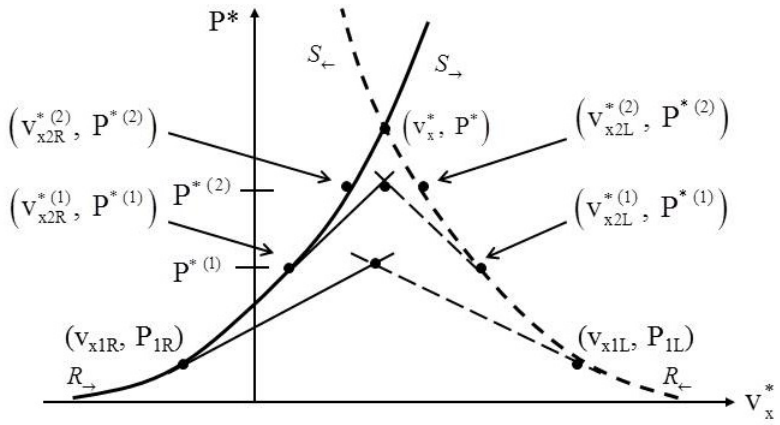

Fig. 5.17 shows the first two iterations in the convergence of the Newton-Raphson based root solver for the Riemann problem. The adiabats associated with the right-going and left-going shocks are shown by the solid and dashed curves. The solid and dashed lines show the tangents to the corresponding curves. The point of intersection of the solid and dashed lines at each iteration yield the pressure that is used for the next iteration.

The x-velocity v_{x2R}^{*} behind the right-going shock or rarefaction can be specified by using eqns. (5.32) and (5.56) to get:

$$v_{x2R}^{*} = v_{x1R} + \left(P^{*} - P_{1R}\right) \Big/ W_R\left(P^{*}\right) \tag{5.66}$$

where $W_R\left(P^{*}\right)$ can be interpreted as the speed of propagation of the right-going shock or rarefaction wave in Lagrangian coordinates. $W_R\left(P^{*}\right)$ is defined for right-going shocks and rarefactions by:

$$W_R\left(P^{*}\right) = \sqrt{\left[\left(\Gamma - 1\right) P_{1R} + \left(\Gamma + 1\right) P^{*}\right] \rho_{1R} / 2} \quad \text{for } P^{*} \geq P_{1R} \tag{5.67S}$$

$$W_R\left(P^{*}\right) = \sqrt{\Gamma\, P_{1R}\, \rho_{1R}}\; \frac{\left(\Gamma - 1\right)}{2\,\Gamma}\; \frac{1 - \left(P^{*}/P_{1R}\right)}{1 - \left(P^{*}/P_{1R}\right)^{(\Gamma-1)/(2\Gamma)}} \quad \text{for } P^{*} < P_{1R} \tag{5.67R}$$

Similarly, the x-velocity v^*_{x2L} behind the left-going shock or rarefaction can be specified by using eqns. (5.34) and (5.64) to get:

$$v^*_{x2L} = v_{x1L} - \left(P^* - P_{1L}\right) \Big/ W_L\left(P^*\right) \tag{5.68}$$

$W_L\left(P^*\right)$ is defined for left-going shocks and rarefactions by:

$$W_L\left(P^*\right) = \sqrt{\left[\left(\Gamma - 1\right) P_{1L} + \left(\Gamma + 1\right) P^*\right] \rho_{1L} / 2} \quad \text{for } P^* \geq P_{1L} \tag{5.69S}$$

$$W_L\left(P^*\right) = \sqrt{\Gamma\, P_{1L}\, \rho_{1L}}\, \frac{\left(\Gamma - 1\right)}{2\,\Gamma}\, \frac{1 - \left(P^*/P_{1L}\right)}{1 - \left(P^*/P_{1L}\right)^{(\Gamma-1)/(2\Gamma)}} \quad \text{for } P^* < P_{1L} \tag{5.69R}$$

Fig. 5.17 shows the adiabats associated with eqns. (5.66) and (5.68) for the situation shown in Fig. 5.14c which results in right- and left-going shocks. The steps in the iterative solution are also shown in Fig. 5.17. When P^* reaches its converged value we have $v^*_{x2L} = v^*_{x2R} = v^*_x$. Thus the iterative Newton-Raphson root solver is designed to drive $v^*_{x2R} - v^*_{x2L}$ to zero.

The iterative process can be started by setting $P^* = P_{1R}$ and $P^* = P_{1L}$ in eqns. (5.67S) and (5.69S) respectively. This is the first iteration shown in Fig. 5.17 where the intersection of the local tangents to the two adiabats are used to obtain $P^{*(1)}$. Substituting the resultant values for $W_R\left(P_{1R}\right)$ and $W_L\left(P_{1L}\right)$ in eqns. (5.66) and (5.68) respectively, and equating the right hand sides of the two equations, gives us the first iterate $P^{*(1)}$ for P* as:

$$P^{*(1)} = \frac{P_{1L}\, W_R\left(P_{1R}\right) + P_{1R}\, W_L\left(P_{1L}\right) - \left(v_{x1R} - v_{x1L}\right) W_R\left(P_{1R}\right) W_L\left(P_{1L}\right)}{W_R\left(P_{1R}\right) + W_L\left(P_{1L}\right)} \tag{5.70}$$

The above equation gives us a good starting approximation for the pressure in the intermediate state.

We now specify how to take a general n^{th} iterate $P^{*(n)}$ and obtain the $(n+1)^{th}$ iterate $P^{*(n+1)}$. As an example, Fig. 5.17 shows the second iteration after $P^{*(1)}$ has been obtained from the first iteration described in the previous paragraph. We see from that figure that the Newton-Raphson procedure requires us to use two more tangents from points on the adiabats corresponding to $P^* = P^{*(1)}$ to obtain the second iterate $P^{*(2)}$. Fig. 5.17 also shows us that the velocities $v_{x2R}^{*(2)}$ and $v_{x2L}^{*(2)}$ after the second iteration are closer together than the velocities $v_{x2R}^{*(1)}$ and $v_{x2L}^{*(1)}$ after the first iteration. Using the n^{th} iterate for the pressure, $P^{*(n)}$, we obtain the n^{th} iterate for the velocities, $v_{x2R}^{*(n)}$ and $v_{x2L}^{*(n)}$, as follows:

$$v_{x2R}^{*(n)} = v_{x1R} + \left(P^{*(n)} - P_{1R}\right) \Big/ W_R\left(P^{*(n)}\right) \tag{5.71}$$

and

$$v_{x2L}^{*(n)} = v_{x1L} - \left(P^{*(n)} - P_{1L}\right) \Big/ W_L\left(P^{*(n)}\right) \tag{5.72}$$

If we are far from convergence, we will not have $v_{x2R}^{*(n)} \approx v_{x2L}^{*(n)}$ and the iteration will have to be continued further. The $(n+1)^{th}$ iterate $P^{*(n+1)}$ is then obtained by a Newton-Raphson step that is meant to drive $v_{x2R}^{*(n)} - v_{x2L}^{*(n)}$ to zero as follows:

$$0 = v_{x2R}^{*(n)} - v_{x2L}^{*(n)} + \left(P^{*(n+1)} - P^{*(n)}\right)\left(\frac{d\, v_{x2R}^{*(n)}}{d\, P^{*(n)}} - \frac{d\, v_{x2L}^{*(n)}}{d\, P^{*(n)}}\right) \tag{5.73}$$

The derivatives in eqn. (5.73) can be evaluated using eqns. (5.66) and (5.68) while using eqns. (5.67) and (5.69) as supporting equations. For hydrodynamics, they have very

simple expressions that can be written with only a minimal amount of extra computation. Thus we define $Z_R\left(P^{*(n)}\right)$ and $Z_L\left(P^{*(n)}\right)$ as:

$$Z_R\left(P^{*(n)}\right) \equiv 1\Big/\left(\frac{d\, v_{x2R}^{*(n)}}{d\, P^{*(n)}}\right) \text{ and } Z_L\left(P^{*(n)}\right) \equiv -1\Big/\left(\frac{d\, v_{x2L}^{*(n)}}{d\, P^{*(n)}}\right) \tag{5.74}$$

to get

$$Z_R\left(P^{*(n)}\right) = \frac{2\, W_R\left(P^{*(n)}\right)^3}{W_R\left(P^{*(n)}\right)^2 + \left(\rho_{1R}\ c_{s1R}\right)^2} \quad \text{for } P^{*(n)} \geq P_{1R} \tag{5.75S}$$

$$Z_R\left(P^{*(n)}\right) = \rho_{1R}\ c_{s1R} \left(\frac{P^{*(n)}}{P_{1R}}\right)^{\frac{(\Gamma+1)}{(2\Gamma)}} \quad \text{for } P^{*(n)} < P_{1R} \tag{5.75R}$$

and

$$Z_L\left(P^{*(n)}\right) = \frac{2\, W_L\left(P^{*(n)}\right)^3}{W_L\left(P^{*(n)}\right)^2 + \left(\rho_{1L}\ c_{s1L}\right)^2} \quad \text{for } P^{*(n)} \geq P_{1L} \tag{5.76S}$$

$$Z_L\left(P^{*(n)}\right) = \rho_{1L}\ c_{s1L} \left(\frac{P^{*(n)}}{P_{1L}}\right)^{\frac{(\Gamma+1)}{(2\Gamma)}} \quad \text{for } P^{*(n)} < P_{1L} \tag{5.76R}$$

Physically, $Z_R\left(P^{*(n)}\right)$ and $Z_L\left(P^{*(n)}\right)$ can be interpreted as the absolute value of the slopes of the solid and dashed curves in Fig. 5.14. The $(n+1)^{th}$ iterate $P^{*(n+1)}$ is now given by:

$$P^{*(n+1)} = P^{*(n)} - \frac{Z_R\left(P^{*(n)}\right) Z_L\left(P^{*(n)}\right)}{Z_R\left(P^{*(n)}\right) + Z_L\left(P^{*(n)}\right)} \left(v_{x2R}^{*(n)} - v_{x2L}^{*(n)}\right) \tag{5.77}$$

Once $P^{*(n+1)}$ is sufficiently close to its converged value P^*, as evinced by $\left|P^{*(n+1)} - P^{*(n)}\right| \Big/ P^{*(n)}$ having a suitably small value, we can optionally make a small, final improvement to the value of v_x^* as follows:

$$v_x^* = \frac{v_{x2R}^{*(n)} Z_R\left(P^{*(n)}\right) + v_{x2L}^{*(n)} Z_L\left(P^{*(n)}\right)}{Z_R\left(P^{*(n)}\right) + Z_L\left(P^{*(n)}\right)} \tag{5.78}$$

This completes our description of the Newton-Raphson root solver for obtaining the intermediate stats of the Riemann problem.

The Newton-Raphson iteration described above converges very rapidly and only two or three iterations are usually needed even for the strongest of shocks that one is likely to encounter. For problems with only a few shocks in the computational domain, the solution is rather smooth at most zone boundaries. At those boundaries, even the two or three previously mentioned iterations can be dispensed with by simply using eqns. (5.70) and (5.78) to obtain the intermediate state. Once the intermediate state $\left(v_x^*,\ P^*\right)$ is found, we can always use eqns. (5.20) and (5.57) to obtain the densities ρ_{2R}^* and ρ_{2L}^* on either side of the contact discontinuity. The transverse velocities are unchanged on either side of the contact discontinuity.

5.4.3) The Entropy Fix in the Iterative Riemann Solver

The fully evolved Riemann problem now has four constant states, the first to the left of the left-going wave, the second to the right of the left-going wave, the third to the left of the right-going wave and the fourth to the right of the right-going wave. See Fig. 5.2 and Figs. 5.15 and 5.16. The speeds of any right- or left-going shocks in the Riemann problem can be obtained from eqns. (5.33) and (5.35). Likewise, the structure of open right- or left-going rarefaction fans can be deduced by evaluating the speeds of the C_+

and C_- characteristics respectively on both sides of the rarefaction fans. As a result, we can evaluate the location of the four constant states relative to the zone boundary. If any one of those states coincides with the zone boundary, we can use the flow variables from that state to obtain the $\overline{U}^{(RS)}_{i+1/2}$ variables that are to be used in eqn. (5.1) to obtain the physically consistent upwinded fluxes. If the zone boundary is straddled by an open, right-going rarefaction fan, we use eqns. (5.53) to (5.55) to obtain $\overline{U}^{(RS)}_{i+1/2}$. Similarly, if the zone boundary is straddled by an open, left-going rarefaction fan, we use eqns. (5.61) to (5.63) to obtain $\overline{U}^{(RS)}_{i+1/2}$. This prescription of opening out rarefaction fans is followed even when the Riemann solver is based on a two-shock approximation; and it is especially important in such situations. It is known in the literature as entropy enforcement and is an essential step in every type of Riemann solver if it is to produce physically consistent answers.

In the next chapter we will design approximate Riemann solvers for hydrodynamics and MHD that are based on rather different philosophies than the one pursued here. We will find that an entropy enforcement step has to be retained even when using those Riemann solvers.

References

Bazer, J. and Ericson, W.B., *Hydromagnetic shocks*, Astrophysical J., 129 (1959) 758

Ben-Artzi, M., *The generalized Riemann problem for reactive flows*, Journal of Computational Physics, 81 (1989) 70-101

Ben-Artzi, M. and Birman, A., *Computation of reactive duct flows in external fields*, Journal of Computational Physics, 86 (1990) 225-255

Ben-Artzi, M. and Falcovitz, J. *Generalized Riemann Problems in Computational Fluid Dynamics*, Cambridge University Press (2003)

Colella, P., A *Direct Eulerian MUSCL Scheme for Gas Dynamics*, SIAM Journal of Scientific and Statistical Computing, 6 (1985) 104

Colella, P. & Glaz, H.M., *Efficient Solution Algorithms for the Riemann Problem for Real Gases*, Journal of Computational Physics, 59 (1985) 264

Colella, P. & Woodward, P., *The Piecewise Parabolic Method (PPM) for Gas-Dynamical Simulations*, Journal of Computational Physics, 54 (1984) 174

Courant, R. & Friedrichs, K.O., *Supersonic Flow and Shock Waves*, Interscience Publishers Inc., New York (1948)

Dumbser M. and Toro E.F., *On universal Osher–type schemes for general nonlinear hyperbolic conservation laws*. Communications in Computational Physics, 10 (2011) 635–671

Godunov, S.K., 1959, Mat. Sb. 47, 271 ; also Cornell Aeronautical Lab. Translation

Horie, Y., *Shock Wave Science and Technology Reference*, Volume 2, Solids1 (2007) Springer

Hugoniot, H., *Sur la propagation du movement dans les corps et specialement dans les gaz parfaits*, Journal de l'ecole polytechnique, 58 (1889) 125

Jefferey, A. & Taniuti, A. , *Nonlinear Wave Propagation*, Academic Press, New York (1964)

Landau, L.D. & Lifshitz, E.M., *Course of Theoretical Physics, volume 6: Fluid Mechanics*, Second Edition, Elsevier (1987)

Lapidus, A., *A Detached Shock Calculation by Second Order Finite Differences*, Journal of Computational Physics, 2 (1967) 154

Lax, P.D., *Weak Solutions of Nonlinear Hyperbolic Equations and their Numerical Computation*, Communications in Pure and Applied Mathematics, 7 (1954) 159

Lax, P.D., *Hyperbolic Systems of Conservation Laws and the Mathematical Theory of Shock Waves*, SIAM, Philadelphia, Pennsylvania (1972)

Menikoff, R. and Plohr, B.J., *The Riemann problem for fluid flow of real materials*, Reviews of Modern Physics, 61 (1989) 75

Myong, R.S. & Roe, P.L., *On Godunov-type schemes for magnetohydrodynamics, 1. A model system*, Journal of Computational Physics, 147 **(**1998) pp. 545–567

Osher, S. and Solomon, F., *Upwind Difference Schemes for Hyperbolic Systems of Conservation Laws*, Mathematics of Computation, 38(158) (1982) 339

Quirk, J.J., *A Contribution to the Great Riemann Solver Debate*, International Journal of Numerical Methods in Fluids, 18 (1994) 555

Rankine, W.J.M., *On the thermodynamic theory of waves of finite longitudinal disturbance*, Transactions of the Royal Society of London, 160 (1870) 277

Riemann, B., *Uber die Fortpflanzung ebener Luftwellen von endlicher Schwingungsweite*, Abhandlungen der Gesselschaft der Wissenschaften zu Gottingen, Mathematisch-physicalische Klasse 8 (1860) 43

Sod, G.A., *A Survey of Finite Difference Methods for Systems of Nonlinear Hyperbolic Conservation Laws*, Journal of Computational Physics, 27 (1978) 1

Thomas, L.H., *Note on Becker's theory of the shock front*, The Journal of Chemical Physics, 12(11) (1944) 449

Timmes, F.X. & Swesty, F.D., *The Accuracy, Consistency, and Speed of an Electron-Positron Equation of State Based on Table Interpolation of the Helmholtz Free Energy*, Astrophysical Journal Supplement, 126 (2000) 501

Toro, E.F. *Riemann Solvers and Numerical Methods for Fluid Dynamics. A Practical Introduction*, Third Edition, Springer-Verlag, New York (2009)

van Leer, B., *Towards the ultimate conservative difference scheme. IV. A new approach to numerical convection*, Journal of Computational Physics, 23 (1977) 276-299

van Leer, B., *Toward the ultimate conservative difference scheme. V. A second-order sequel to Godunov's method*, Journal of Computational Physics, 32 (1979) 101

van Leer, B., *Computing Methods in Applied Science and Engineering VI*, eds. R. Glowinski and J.-L. Lions, North Holland, Amsterdam, p. 493 (1984)

Woodward, P. & Colella, P., *The Numerical Simulation of Two-dimensional Fluid Flow with Strong Shocks*, Journal of Computational Physics, 54 (1984) pp. 115-173

Zwerger, T. & Muller, E., *Dynamics and Gravitational Wave Signature of Axisymmetric Rotational Core Collapse*, Astronomy & Astrophysics, 320 (1997) 209

Problem Set

5.1) a) Recalling the Lax entropy condition from the previous chapter, show that physical entropy is increased as the fluid flows through a compressive shock. Do this by picking $\rho_1 = 1$, $P_1 = 1$, $\Gamma = 1.4$ and $P_2 = 4$ for the compressive shock. Then use eqn. (5.20) to obtain ρ_2 for the post-shock density. Show that the post-shock entropy increases for the

compressive shock. **b)** Now show that the entropy decreases as the fluid flows through an unphysical rarefaction shock. Do this by picking $\rho_1 = 1$, $P_1 = 1$, $\Gamma = 1.4$ and $P_2 = 0.2$ for the rarefaction shock. Again, use eqn. (5.20) to obtain ρ_2 for the post-shock density. Then show that the post-shock entropy decreases for the rarefaction shock.

5.2) a) Again recalling the Lax entropy condition from the previous chapter, show that the right-going characteristics flow into a physical, i.e. compressive, right-going shock. Do this by picking $\rho_1 = 1$, $P_1 = 1$, $\Gamma = 1.4$ and $P_2 = 4$ for the compressive shock. Then use eqn. (5.20) to obtain ρ_2 for the post-shock density and then use eqns. (5.23) and (5.24) to obtain u_{x1} and u_{x2} . Recall that these velocities are negative in the right-going shock's rest frame. Show that in the shock's frame, the characteristics with speeds $u_{x1} + c_{s1}$ and $u_{x2} + c_{s2}$ flow into the compressive shock. **b)** On the other hand, show that the right-going characteristics flow out of a right-going rarefaction shock. Do this by picking $\rho_1 = 1$, $P_1 = 1$, $\Gamma = 1.4$ and $P_2 = 0.2$ for the rarefaction shock. Again, use eqn. (5.20) to obtain ρ_2 for the post-shock density and then use eqns. (5.23) and (5.24) to obtain u_{x1} and u_{x2} . Show that in the shock's frame, the characteristics with speeds $u_{x1} + c_{s1}$ and $u_{x2} + c_{s2}$ flow away from the rarefaction shock.

5.3) Consider a straight tube that is filled with gas having unit density, unit pressure and $\Gamma = 5/3$. The gas is initially at rest. A piston that is initially at rest is placed in the tube at x=0. We are interested in the gas flow that develops in the region with x>0. At time t=0 the piston is plunged to the right with a uniform, unit velocity. In the process, a shock propagates to the right of the piston. a) Find the density, pressure and velocity of the shocked fluid. b) Find the shocked velocity relative to the unshocked fluid.

5.4) Consider a right-going shock that is initially at x<0 and moving toward a stationary, reflecting wall that is located at x=0. The unshocked fluid that lies between the initial shock and the wall has unit density, unit pressure, $\Gamma = 5/3$ and is initially at rest. The shock moves at a speed of two units relative to the unshocked fluid. a) Find the post-

shock density, pressure and velocity before the shock reaches the wall. b) After the shock has reflected off the wall, find the density and pressure at the wall as well as the velocity with which the shock propagates away from the wall.

5.5) Consider a straight tube that is filled with gas having unit density, unit pressure and $\Gamma = 5/3$. The gas is initially at rest. A piston that is initially at rest is placed in the tube at x=0. At time t=0 the piston starts moving to the left with a uniform, unit velocity. What are the values of the density, pressure and x-velocity of the flow at x=0 for times t>0.

Computational Exercises

5.1) Using the Riemann solver provided on the CD-ROM, construct a one-dimensional code for solving the Euler equations. Use the limiters that are also provided in the CD-ROM. The minmod or van Leer limiters are perfect for this project. Use the time-stepping scheme shown in eqns. (3.50) and (3.51) to construct a spatially and temporally second order, one-dimensional Euler flow code. Do this using the following steps:

i) First declare one-dimensional array variables for the solution variables. We use conserved variables as our solution variables and they consist of mass, momentum and energy densities defined at the zone centers of our one-dimensional mesh. Remember to leave a few extra zones (2 to 4 will do) on either side of the computational domain to hold the boundary information that may need to be refreshed at each timestep. (For the Riemann problems in the next problem, even this process of refreshing the boundary zones is not needed.) Realize that eqns. (3.50) and (3.51) pertain to a two step scheme. As a result, you will have to retain an old and new set of arrays for all the U_i^n and U_i^{n+1} solution variables. You will also need to have further array variables that contain a discrete representation of the rates of update for the solution variables.

ii) From eqns. (3.50) and (3.51) realize that we want a subroutine that accepts one-dimensional array variables for the mass, momentum and energy densities and returns a discrete version of their rates of update. Thus we want to come out of this subroutine with

an evaluation of $\left(\mathrm{F}_{i+1/2}^{(RS)} - \mathrm{F}_{i-1/2}^{(RS)}\right)\Big/\Delta x$ for each zone "*i*", i.e. the entire set of one-dimensional arrays that went into the subroutine. This is done as follows:

ii.a) Once inside the subroutine, construct arrays of primitive variables, i.e. density, velocities and pressure, from the conserved variables. I.e. for each vector U_i in each zone, construct a corresponding vector V_i .

ii.b) Construct arrays that hold the undivided differences of the primitive variables, $\Delta\mathrm{V}_i$. Do this by using the limiters from the previous chapter.

ii.c) Use the primitive variables and their slopes on either side of each zone boundary to construct variables to the left of the zone boundary $\left(\rho_{1\mathrm{L}}, \mathrm{v}_{\mathrm{x1L}}, \mathrm{v}_{\mathrm{y1L}}, \mathrm{v}_{\mathrm{z1L}}, \mathrm{P}_{1\mathrm{L}}\right)^T \equiv \mathrm{V}_i + \Delta\mathrm{V}_i / 2$ and the corresponding flow variables to the right of the zone boundary $\left(\rho_{1\mathrm{R}}, \mathrm{v}_{\mathrm{x1R}}, \mathrm{v}_{\mathrm{y1R}}, \mathrm{v}_{\mathrm{z1R}}, \mathrm{P}_{1\mathrm{R}}\right)^T \equiv \mathrm{V}_{i+1} - \Delta\mathrm{V}_{i+1} / 2$. Do this for all zone boundaries so that we have one array for each of the left variables and, similarly, one array for each of the right variables.

ii.d) Send arrays of left and right variables to the Riemann solver. Think of the Riemann solver as a machine that uses the information provided to return properly upwinded fluxes $\mathrm{F}_{i+1/2}^{(RS)}$ for each zone boundary "*i*+1/2".

ii.e) Use the fluxes $\mathrm{F}_{i+1/2}^{(RS)}$ to evaluate rates of update $\left(\mathrm{F}_{i+1/2}^{(RS)} - \mathrm{F}_{i-1/2}^{(RS)}\right)\Big/\Delta x$. Now return from this subroutine with the properly evaluated rates of update.

iii) Now incorporate a time update strategy consistent with eqns. (3.50) and (3.51). Do this using a loop that integrates forward in time for a desired number of time steps. Each iteration of that time step loop should have two parts. The first part takes a predictor step $\mathrm{U}_{\mathrm{i}}^{\mathrm{n+1/2}} = \mathrm{U}_{\mathrm{i}}^{\mathrm{n}} - \dfrac{\Delta t}{2\,\Delta x}\left(\mathrm{F}_{RS}\left(\mathrm{U}_{L;i+1/2}^{n}, \mathrm{U}_{R;i+1/2}^{n}\right) - \mathrm{F}_{RS}\left(\mathrm{U}_{L;i-1/2}^{n}, \mathrm{U}_{R;i-1/2}^{n}\right)\right)$ with time step $\Delta t/2$. The second part takes a corrector step $\mathrm{U}_{\mathrm{i}}^{\mathrm{n+1}} = \mathrm{U}_{\mathrm{i}}^{\mathrm{n}} - \dfrac{\Delta t}{\Delta x}\left(\mathrm{F}_{RS}\left(\mathrm{U}_{L;i+1/2}^{n+1/2}, \mathrm{U}_{R;i+1/2}^{n+1/2}\right) - \mathrm{F}_{RS}\left(\mathrm{U}_{L;i-1/2}^{n+1/2}, \mathrm{U}_{R;i-1/2}^{n+1/2}\right)\right)$ with time step Δt. Notice that in the corrector step we can overwrite $\mathrm{U}_{\mathrm{i}}^{\mathrm{n}}$ with $\mathrm{U}_{\mathrm{i}}^{\mathrm{n+1}}$ for each zone "i". Also evaluate a new time step Δt for the next iteration, consistent with the Courant condition.

5.2) Use the code from the previous problem to solve a few of the Riemann problems described below. Use the flow solver described above with a mesh with about 100 to 400 zones covering the unit interval [–0.5, 0.5]. The results should match up with the solutions shown in Figs. 5.15 and 5.16 wherever appropriate.

i) Sod (1978) shock problem:

$$\begin{aligned} (\rho, P, v_x) &= (1, 1, 0) \qquad \text{for } x<0 \\ &= (0.125, 0.1, 0) \qquad \text{for } x>0 \end{aligned}$$

Use $\Gamma = 1.4$ for this problem. The problem should be stopped at a time of 0.2. The result is shown in Fig. 5.15a.

ii) A problem that is quite similar to the Sod problem is the Lax (1954) problem:

$$\begin{aligned} (\rho, P, v_x) &= (0.445, 3.528, 0.698) \qquad \text{for } x<0 \\ &= (0.5, 0.571, 0) \qquad \text{for } x>0 \end{aligned}$$

Use $\Gamma = 1.4$ for this problem. The problem should be stopped at a time of 0.13.

iii) One half of the Woodward & Colella (1984) problem:

$$\begin{aligned} (\rho, P, v_x) &= (1.0, 0.01, 0) \qquad \text{for } x<0 \\ &= (1.0, 1000.0, 0) \qquad \text{for } x>0 \end{aligned}$$

Use $\Gamma = 1.4$ for this problem. The problem should be stopped at a time of 0.01. The result is shown in Fig. 5.15b.

iv) Two strongly supersonic colliding streams of very low pressure gas:

$$\begin{aligned} (\rho, P, v_x) &= (1.0, 0.2, 2.0) \qquad \text{for } x<0 \\ &= (1.5, 0.2, -2.0) \qquad \text{for } x>0 \end{aligned}$$

Use $\Gamma = 5/3$ for this problem. The problem should be stopped at a time of 0.4. The result is shown in Fig. 5.16a. The reader will see a slightly greater post-shock oscillation in his or her result. The oscillations stem from the fact that the problem has extremely strong shocks that move very slowly with respect to the mesh. The result shown in Fig. 5.16a uses a small amount of Lapidus (1967) viscosity to damp out those oscillations.

v) Two strong rarefaction fans:

$$\begin{aligned} (\rho, P, v_x) &= (1.0, 2.0, -2.5) \qquad \text{for } x<0 \\ &= (1.5, 4.0, 2.5) \qquad \text{for } x>0 \end{aligned}$$

Use $\Gamma = 5/3$ for this problem. The problem should be stopped at a time of 0.08. The result is shown in Fig. 5.16b. We see a small dimple in the density at the contact discontinuity. This is a region of slightly higher entropy and is initially needed by the numerical method to resolve the Riemann problem in an entropy satisfying fashion. However, once the dimple is produced, the numerical method treats it as a flow feature and never gets rid of it.